

Graph-based Analysis for Revealing the Stochastic Gravitational Wave Background in Pulsar Timing Arrays

M. Alakhras^{1,2,*} and S. M. S. Movahed^{1,3,4,†}

¹*Department of Physics, Shahid Beheshti University, 1983969411, Tehran, Iran*

²*Department of Physics, Faculty of Sciences, Damascus University, Damascus, Syria*

³*School of Astronomy, Institute for Research in Fundamental Sciences (IPM), P. O. Box 19395-5531, Tehran, Iran*

⁴*Department of Mathematics and Statistics, The University of Lahore, 1-KM Defence Road Lahore-54000, Pakistan*

(Dated: September 30, 2025)

The stochastic gravitational wave background (SGWB) reveals valuable information about its origin and the Universe. The pulsar timing arrays (PTAs) are suitable indicators for detecting SGWB within the nano-Hertz frequency range. In this work, we propose a graph-based method implemented on the pulsar timing residuals (PTRs) for SGWB detection and examining uncertainties of its parameters. We construct a correlation graph with pulsars as its nodes, and analyze the graph-based summary statistics, which include topological and geometrical characteristics, for identifying SGWB in real and synthetic datasets. The effect of the number of pulsars, the observation time span, and the strength of the SGWB on the graph-based feature vector is evaluated. Our results demonstrate that the merit feature vector for common signal detection consists of the average clustering coefficient and the edge weight fluctuation. The SGWB detection conducted after the observation of a common signal and then exclusion of non-Hellings & Downs templates is performed by the second cumulant of edge weight for angular separation thresholds $\bar{\zeta} \gtrsim 40^\circ$. The lowest detectable value of SGWB strain amplitude utilizing our graph-based measures at the current PTAs sensitivity is $A_{\text{SGWB}} \gtrsim 1.2 \times 10^{-15}$. Fisher forecasts confirmed that the uncertainty levels of $\log_{10} A_{\text{SGWB}}$ and spectral index reach 2.2% and 28.3%, respectively, at 2σ confidence interval. Evidence for an SGWB at the 3σ level is obtained by applying our graph-based method to the NANOGrav 15-year dataset.

I. INTRODUCTION

For an extended period, electromagnetic waves served as the undisputed benchmark for conveying information throughout the Universe. Consequently, by enhancing observational capabilities, serendipitous discoveries were made, including e.g. the observation of relic radiation from hot Big Bang phenomenon [1, 2], as well as large-scale-structures (LSS) [3, 4] and exotic electromagnetic sources including gamma-ray bursts [5, 6], X-ray binary systems [7, 8], pulsars [9, 10] and quasi-stellar objects [11], among others. Gravitational wave (GW) which is the direct prediction of Einstein's theory of general relativity [12, 13], furthermore, open a distinct window onto the exploring the fundamental nature of Universe [14–18, and references therein]. The LIGO collaboration's direct detection of gravitational wave from the merger of two black holes in 2015 [19] presented an encouraging opportunity for assessing the fabric of the Universe through the propagating ripples in the curvature of spacetime.

The GWs produced by resolved sources through space-time distortions such as compact binary mergers in the strong-field and relativistic regime with typical frequencies of $f \sim [\text{mHz} - \text{kHz}]$ or individual supermassive black hole binaries ($f \sim \text{nHz}$) are not the sole form of gravitational radiation. From a fundamental perspective, there

is no longer doubt for existing a mechanism whereby the superposition of numerous independent and unresolved gravitational wave signals, regardless they originate from cosmological or astrophysical sources, can occur [20]. This specific type of GW which may be treated by non-deterministic strain signals is known as the stochastic gravitational wave background (SGWB) [17, 21, 22]. The SGWB is ubiquitous feature that can be generated in many theories, including cosmological inflation [23–28, and references therein], primordial phase transitions [29–36], modified gravity theories [15, 18, 37, and references therein], theories that go beyond the standard model of particles [17, 18, 38] and the superposition of enormous number of unresolved astrophysical GW events [20]. Analogous to the CMB, the SGWB are moving through the Universe, providing a complementary observational tool that exhibits a significant difference from the CMB. In fact, the SGWB can propagate through free streaming once generated, whereas electromagnetic waves are altered by various collision mechanisms, resulting in their onset of free streaming only after recombination ($z_{\text{rec}} \sim 1100$).

The foundation of remarkable accomplishments in understanding such faint waves is comprised of model construction that relies on either phenomenological descriptions or fundamental principles, together with observational pipelines and simulation suites.

Thanks to numerous observational surveys designed to probe the Universe, high-precision collections of datasets with multidimensional nature have become accessible. For the sake of completeness, one might iden-

*Electronic address: m.alakhras@sbu.ac.ir

†Electronic address: m.s.movahed@ipm.ir

tify some of the currently operational, ongoing, and planned surveys that are either focused on or apart of their missions dedicated to the detection of GWs, such as: LISA (Laser Interferometer Space Antenna)¹ [39], LIGO-Virgo-KAGRA² [40], Einstein Telescope (ET) [41], Deci-hertz Interferometer Gravitational Wave Observatory (DECIGO) [42], Cosmic Explorer (CE) [43, 44], the North American Nanohertz Observatory for Gravitational Waves (NANOGrav)³ [45–48], the Parkes Pulsar Timing Array (PPTA)⁴ [49–52], the European Pulsar Timing Array (EPTA)⁵ [53, 54], the Indian PTA (InPTA)⁶ [55], and the International Pulsar Timing Array (IPTA)⁷ [56, 57]. Looking ahead, key radio facilities that will significantly enhance PTA sensitivity include the Square Kilometre Array (SKA) [58–60] and the Five-hundred-meter Aperture Spherical radio Telescope (FAST) [61]. Furthermore, an intensive explanation about the details of frequency band for GW detection can be found in [62].

The development of numerous simulation suites to generate synthetic GW over different frequency ranges [63, 64] has encouraged researchers to employ field-level inferences and to introduce more sophisticated summary statistics for evaluating the detection pipeline, subsequently enabling cosmological inferences. A list of some famous suites for GW mock data simulations and analysis toolkits are: LALSuite⁸ [65], BILBY⁹ [66], Legacy LISA Code [67], Bayesian PTA analysis with GW signal injection (ENTERPRISE)¹⁰ [68], TEMPO2¹¹ [69], PINT¹² [70], reconstructing the spectral shape of GWB (GWBackFinder)¹³ [71], CLASS-GWB [72], Gravitational Wave Universe Toolbox [73] and Einstein Toolkit [74].

The synergies between GW and other probes such as LSS (matter density fields, halos and galaxy surveys), 21-cm intensity and lensing maps presents a valuable opportunity yielding promising approach for both putting pristine constraints on cosmological parameters and either reducing or removing degeneracies between them. A pioneer task for aforementioned idea including the terminology such as “standard sirens” was proposed by [75], and after that followed by many researchers e.g. [76–85, and references therein]. Intensive evaluations for mutual information between GW and LSS was done in successive

works by [86–90]. It is worth mentioning that, after highlight the Λ CDM tensions and anomalies for LSS (see e.g. [91–93], and references therein) introducing new pipelines incorporating GW, especially SGWB has been utilized to examine the anisotropy and asymmetry of Universe [94–96], evaluating w_0 , H_0 and σ_8 tensions as well as interaction between dark sectors of Universe [78, 83, 97–99]. The magneto-hydrodynamic turbulence can mainly produce magnetic stress tensor components [100–102] and it is subsequently the source of metric tensor perturbations which produces the GW. This idea mainly has been exemplified in various researches such as [17, 103–105]. The connection between Primordial Black Hole (PBH) and GWs has been examined in different papers (see e.g. chapter 5 of [106], and references therein). Observational constraints on the tension of cosmic string from emitting GW has been reported in [36, 48, 107–110, and references therein].

As a result, the combination of GW with other types of signals (Multi-messenger Astronomy) for probing both early and late Universe and revealing invisible phenomena in our cosmos, along with considerable improvements in observational facilities, has spurred massive interest in the subject of GW, especially the SGWB.

In principle, the space-based detectors [39], ground-based detectors [40], CMB B-modes [2, 111, 112] and PTAs [48] are most relevant methods for exploring SGWB with their own frequency sensitivities. The optimal data analysis for identifying the signature of space-time tiny distortion and therefore performing cosmological inferences and associated constraints on the fundamental physics depend on adopted survey and type of observed datasets.

Robust learning from noisy, incomplete, and relatively sparse data, especially those series that exemplify GW, can be achieved by seamlessly integrating data with physical priors, such as physical laws, principles, constraints, and symmetry, a methodology known as Physics-Informed Machine Learning [113, 114]. A common approach to take into account the physical priors is making the proper feature vector. A pioneer research has been done by [115]. In pursuit of quality enhancement in GW data, various approaches have been recognized, encompassing the reconstruction of GW signals, accurate assessment of statistical and systematic errors, as well as the identification, fast signal characterization, robustly have been noticed in [116, and references therein]. GWB from binary black hole mergers [117], Noise reduction in GW data [118, 119], localization of a GW source through machine learning (ML) [120–122] are just a short list of studies representing the promising of ML applications in GW physics. A recent overview for GW research with current interferometric detectors is given by [123]. Component separations (noise and signal), likelihood free parameter estimations, source identification and performing field-level inferences can reliably conducted by so-called Simulation-Based-Inference (SBI) approach [124–128, and references therein], and it is undoubtedly cru-

¹ <https://www.lisamission.org/>

² <https://ligo.org/>

³ <https://nanograv.org/>

⁴ <https://www.atnf.csiro.au/>

⁵ <https://www.epta.eu.org>

⁶ <https://inpta.iitr.ac.in/>

⁷ <https://ipta4gw.org/>

⁸ <https://lscsoft.docs.ligo.org/lalsuite/lalsuite/index.html>

⁹ <https://github.com/bilby-dev/bilby>

¹⁰ <https://enterprise.readthedocs.io/en/latest/>

¹¹ <https://bitbucket.org/psrsoft/tempo2/src/master/>

¹² <https://github.com/nanograv/PINT>

¹³ <https://github.com/AndronikiDimitriou/GWBackFinder>

cial and necessary for upcoming generation of both space- and ground-based facilities that are focused on GW sky [129].

Millisecond radio pulsars (MPs), which are emitting intensive coherent electromagnetic radio wave is particular class of pulsars. They have very stable rotational period leading to one of suitable indicators for revealing SGWB transiting between earth and pulsar timing arrays (PTAs). The random distribution of pulsars in the sky makes the PTA as a possible detector with astrophysical arm length size to identify very low frequency GW ($f \in [10^{-9} - 10^{-7}]$ Hz) [48]. The operating frequency of PTA lies in the frequency range of SGWB generated by cosmological and astrophysical phenomena. The continuous waves from individual binaries is also in the detectability range of PTA. According to the recent results, the cosmological interpretation of the SGWB signal is favored over the more conventional explanation involving supermassive black hole binaries (SMBHBs) [48]. However, such results rely on specific modeling assumptions adopted for the cosmic SMBHB population.

The stochastic nature of gravitational wave background is intrinsically convolved with those arising from unresolved sources and influenced by various unknown phenomena during its propagation, in addition to systematic noise. Subsequently, to elucidate the physics of SGWB, detection strategies and then cosmological inferences must be accurately designed to facilitate reliable breakthrough. A powerful approach for quantification of the SGWB as a generic cosmological field ¹⁴ is necessarily relying on the principle of stochastic field [137, 138]. Generally a stochastic field denoted by $\mathfrak{F} = \{\mathcal{F}_j \mid \mathcal{F}_j : \Pi_j \rightarrow \mathbb{R}, \Pi_j \subset \mathbb{R}^D\}_{j=1}^d$ is defined by a measurable mapping from probability space into a σ -algebra of \mathbb{R}^d -valued function on \mathbb{R}^D -Euclidean space [139]. A complete description of $\mathcal{F}^{(d+D)}$ can be treated by evaluating *shape, size, boundary and connectedness* under the banner of morphology and it is systematically manifested by Minkowski Functionals (MFs) in their either scalar or tensor forms [140–148, and references therein]. To extend their merit, recently the weighted morphological measures has been proposed in [149, 150]. The intersection of algebraic topology and computational geometry enhanced by sophisticated algorithms, provides unrivaled sets in data generated by a collections of ambitious projects in cosmology [151–153, and references therein].

For detecting GW by PTA, the residual signal - the difference between measured and predicted time of arrivals (TOAs) - is calculated [57]. The Pulsar Timing Residuals (*PTRs*) are very sensitive indicators to elucidate interesting physical properties of pulsars and other cosmological and astrophysical foreground processes [52, 154, 155].

¹⁴ One can point out to other kinds of field particularly in cosmology such as Cosmic Microwave Background (CMB) [130–135]; the LSS of the Universe [3, 4, 136].

It is essential to thoroughly elucidate the different components associated with the modeling of deterministic contributions to arrival times, the stochastic astronomical and instrumental delays, and eventually the elimination of systematic errors [156]. It has become evident that preparing appropriate catalog of pulsars for subsequent inferences necessitates the incorporation of sophisticated data pre-processing. Motivated by these discrepancies and inspired by advances in data analysis routines, several researchers have investigated *PTRs* to identify SGWB and estimate its physical parameters.

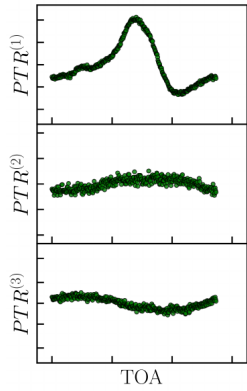
Searching the quasi-quadrupole spatial cross-correlation of PTA reveals the unique signature of SGWB, and it was the pioneering approach used by Hellings & Downs [157, 158]. Inspired by the concept of self-similarity, [155] introduced an innovative approach for irregular fluctuation analysis, which is a suitable method for both SGWBs detection and even for discriminating between different sources of GW. Finally, they also established an upper bound on the characteristic strain amplitude [155]. Resolving bright individual SMBHBs in the presence of SGWB through future PTAs has been examined in [159]. Extracting the relevant physical observables from power spectrum and overlap reduction function (Hellings & Downs curve) in PTA was carried out by [160]. Various kinds of data are recorded through observational surveys and they can be classified into *time series, field, point cloud and graph* [153]. Some mappings between aforementioned classes to make them appropriate for further analysis are known as *recurrent plot* for multi-variable time series to field [161–164], *time delay embedding* [165, 166] and *state-space* [167–169] for transferring the time-series to point cloud, *visibility graph* [170] and *correlation graph* [171], *ordinal partition graph* [172, 173], *proximity graph, cycle graph, recurrence graph* and *transition graph* methods for conversion time series to graphs [174–176, and references therein].

For our case study, i.e. PTAs, we have multi-variable time series in $(N_{\text{PTA}} + 1)$ -dimension. Assuming the N_{PTA} is the number of observed pulsars and for each we have recorded *PTRs* time series denoted by $PTR^{(a)}(t_i)$ such that $i = 1, \dots, M$ and $a = 1, \dots, N_{\text{PTA}}$ ¹⁵. In terms of general definition of stochastic field, we instead have multi-variable time series in $(N_{\text{PTA}} + 1)$ -dimension as [177]:

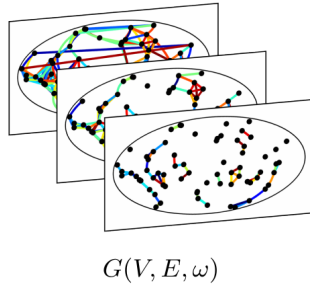
$$PTRs \equiv \left\{ PTR^{(a)}(t_i) \right\}_{(i=1, a=1)}^{(M, N_{\text{PTA}})} \quad (1)$$

¹⁵ In practical scenario, the timestream exhibits irregularities over the time, which implies that $\Delta t_i \equiv |t_{i+1} - t_i|$ depends on the index i . This irregularity introduces certain discrepancies in data analysis. For the sake of generality, we will now assume that synthetic data for all pulsars are regular, possessing the same time interval [155]. The term of irregularity is also referred to *Poisson, intermittent* and *Gaussian* regimes as pointed out by [62].

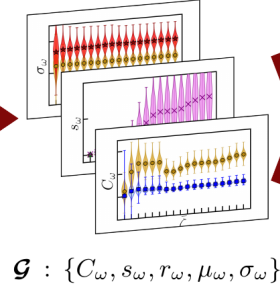
Synthetic/Observed Data



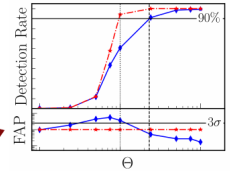
Graph Construction



Summary Statistics



Statistical Inference



Uncertainty Propagation

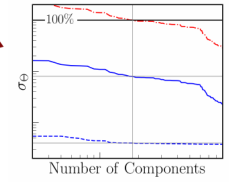


FIG. 1: The proposed data-driven pipeline for PTA data analysis using graph-theory. Timing residuals, $PTRs$, are converted into complex networks, from which graph-based summary statistics are extracted. These features are used to detect the SGWB and to evaluate uncertainties of parameters.

The graph theory as an informative tool for characterizing observations in cosmology has been utilized, particularly in the context of cosmic web analysis [178, 179]. This theory has also been used for the classification of MPs [180] and in the visualization of pulsar population [181]. The topology of pulse profiles of pulsars was explored by constructing a complex network [182]. In this study, inspired by the approach mentioned above to reveal hidden information in multi-variable time series and to assess a data-driven method for the detection of SGWB, we would construct complex networks for both synthetic and real PTA. Subsequently, we inspect the sensitivity of several topological and geometrical features of *a priori*¹⁶ the constructed graph, including average clustering coefficient, average node strength, general assortativity coefficient, the mean edge weight, and the standard deviation of edge weights to the presence of SGWB. We show that this approach leads to consistent constraints of associated parameters: characteristic strain amplitude (A_{SGWB}), and spectral index (γ_{SGWB}) with traditional Bayesian technique.

From detectability perspective for SGWB, in principle, it is crucial to examine the reliability and robustness of proposed pipeline including the sequences of data analysis and associated measured through synthetic datasets before implementing them to the observational data. A comprehensive approach to deal with the $PTRs$ for searching the SGWB should incorporate at least the following parts:

- 1) Generating synthetic $PTRs$ in the presence of SGWB imprint with more realistic systematic noise, and foreground;
- 2) Adopting robust algorithms for data reduction and

data analysis;

- 3) Proposing the specific summary statistics, determining corresponding theoretical descriptions and numerical algorithms, to achieve robust computational results. Also the suitable numerical estimators should be adopted¹⁷;
- 4) Computing the significance of SGWB detection - the minimum value of SGWB amplitude which is uniquely distinguished from other portions of mock data - thereby demonstrating the capability of detection;
- 5) Forecasting the uncertainty of model free parameters according to the given feature vector is conducted before dealing with observed data;
- 6) Implementation of the proposed pipeline on the observed $PTRs$ data to assess the presence of SGWB and therefore estimate or put an upper bound¹⁸ on the strain amplitude;
- 7) Performing either likelihood-based or Simulation-based inferences to put stringent constraints on the desired astrophysical and cosmological parameters which are relevant to SGWB¹⁹.

In view of the previously discussed tasks, we outline

¹⁶ We commence by presuming physics-informed graph fabrication.

¹⁷ The field-level inference can be used instead of summary statistics, when the forward modeling and huge amount of training sets are available [183–185].

¹⁸ The lower bound is appropriate when synthetic data sets are employed to explain the detection performance of certain summary statistics, as illustrated in this study.

¹⁹ As discussed in the text, in the absent of explicit theoretical relation between summary statistics and model free parameters, one can employ the appropriate emulator such as Gaussian process emulator [186] to infer the best fit values and associated confidence intervals for parameters. In the context of SBI, the neural estimator can play the same role [124–128, and references therein].

the main novelties and advantages of our research as follows:

I) We carefully simulate *PTRs* affected by a scenario of SGWB and noise, with red noise component superimposed to construct as most as like realistic data for various values of model parameters. Relying on the graph theory, the complex network from *PTRs* of pulsars distributed in our celestial sphere, will be created.

II) Given the fact that the effect of SGWB is highly degenerated by red noise and other foreground phenomena, the HD curve is investigated as the main potential indicator of SGWB footprint.

III) A comprehensive pipeline is proposed to ensure the input *PTRs* is adequately prepared for the implementation of our exclusive summary statistics based on graph theory (Fig. 1).

IV) Also, the significance of detecting the SGWB signal produced by astrophysical sources (SMBHB) captured through PTA will be assessed from the perspective of the topology and geometry of the constructed complex network by computing the *AUC*, Welch's *t*-test *p*-value and Cohen's *d* metrics. Additionally, we will explore how the number of pulsars, total observation time span and the SGWB strength affect the capability of detection, along with the uncertainties associated with the SGWB strain amplitude and spectral index.

V) According to our graph-based analysis, we will assess their constraining capability on the SGWB parameters by performing the Fisher information matrix analysis.

VI) Finally, we implement our graph-based method on NANOGrav 15-year dataset.

The main objectives of this research are to test our graph-based approach for detectability of SGWB when we are dealing with indirect approach, namely imprint of SGWB on the *PTRs*. Investigating the uncertainty levels of model free parameters, using the summary statistics which includes topology and geometry of complex networks constructed from *PTRs*, will be another part of our purposes. We argue that the SGWB would be detected at high significance through the graph measures. Namely the edge weights standard deviation distinguish the GW imprint from other correlation models sourced by observatory clock errors or solar system ephemeris errors. We also advocate using the graph-based approach alongside of the Bayesian likelihood analysis or the frequentist optimal statistic to constrain the strain amplitude and spectral index of SGWB, making it a new and valuable element of the summary statistics utilized in the SBI approach.

The rest of the paper is organized as follows: in Sec. II, we will give a bird eye on the SGWB from theory to corresponding imprints on the PTA data. Sec. III is devoted to data description for both synthetic and observed PTA data. The details of generating mock PTA data for various sources of SGWB, which include instrumental and foreground noises is also given in this section. We will elucidate the details of complex network construction and subsequently the derived quantities, the

imprint of SGWB on the graph-based summary statistics of PTA data, alongside the scaling effects in Sec. IV. In Sec. V, we will quantify the information content of graph-based analysis to detect SGWB using real PTA data of NANOGrav 15-year data release. The uncertainty on A_{SGWB} and γ_{SGWB} from Fisher forecasts will be computed in Sec. V. We will give our summary and conclusion in Sec. VI.

II. A BRIEF ON THEORETICAL FOUNDATION OF SGWB ON PTA

As mentioned in the introduction, the SGWB is the superposition of GWs produced by numerous unresolved astrophysical and/or cosmological sources with incoherent temporal phases which is statistically isotropic and Gaussian²⁰. The mathematical description of SGWB regardless of their astrophysical and cosmological origin, is treated by metric perturbations in linearized regime as $g_{\mu\nu} = \eta_{\mu\nu} + h_{\mu\nu}$. The spatial perturbation, h_{ij} , is written as:

$$h_{ij}(t, \mathbf{r}) = \int_{-\infty}^{+\infty} df \int_{\mathbb{S}^2} d\hat{n} \sum_{\diamond=+, \times} h_{\diamond}(f, \hat{n}) \epsilon_{ij}^{\diamond}(\hat{n}) e^{i2\pi f(\frac{\hat{n}\cdot\mathbf{r}}{c} - t)} \quad (2)$$

where $\epsilon_{ij}^{\diamond}(\hat{n})$ is the polarization base tensor [187]. The energy density of GW is $\rho_{\text{GW}} \equiv c^2 \langle \dot{h}_{ij} \dot{h}^{ij} \rangle / 32\pi G$, and accordingly, the GW energy density frequency spectrum integrated over solid angle, $d\hat{n}$, is defined as [18]:

$$\Omega_{\text{GW}}(f) \equiv \frac{1}{\rho_c} \frac{d\rho_{\text{GW}}(f)}{d \ln f} \quad (3)$$

with $\rho_c \equiv 3c^2 H_0^2 / 8\pi G$. The 'one-sided' strain spectrum, $S_h(f)$, reads as:

$$S_h(f) \equiv 2 \int_{\mathbb{S}^2} d\hat{n} \sum_{\diamond=+, \times} \langle h_{\diamond}(f, \hat{n}) h_{\diamond}^*(f, \hat{n}) \rangle \quad (4)$$

And the characteristic strain spectrum is $h_c(f) \equiv \sqrt{f S_h(f)}$. Thus the energy density can be written in terms of strain spectrum as:

$$\Omega_{\text{GW}}(f) = \frac{\pi c^2 f^3}{4\rho_c G} S_h(f) \quad (5)$$

Also, in terms of characteristic strain spectrum, we have:

$$\Omega_{\text{GW}}(f) = \frac{\pi c^2 f^2}{4\rho_c G} h_c^2(f) \quad (6)$$

²⁰ According to the cosmological principle, we anticipate to have an isotropic background. One can consider a weak anisotropy for an astrophysical SGWB due to the non-uniform sky distribution of SMBHB which we don't treat in this paper. A non-Gaussian signature is reasonable if at least one of the connected *n*-point correlation functions (cumulants) for $n \geq 3$ is non-zero.

TABLE I: Summary of synthetic and observational PTA parameters.

Component	Parameter	Mock PTA	Real PTA	Description
Pulsar Array	N_{PTA}	68	68	Total number of pulsars
	T_{span}	15 years	16 years	Total observation duration
	Δt	2 weeks	1–4 weeks	Time between observations
	Sky distribution	Uniform	Non-uniform	–
White Noise	$\sigma^{(a)}$	[100, 1000] ns	[50, 5000] ns	Noise strength per pulsar
Red Noise	$A_{\text{rn}}^{(a)}$	$[10^{-15}, 10^{-13}]$	$[10^{-17}, 10^{-13}]$	Strain amplitude at $f_{\text{ref}} = 1/\text{yr}$
	$\gamma_{\text{rn}}^{(a)}$	[2, 5]	[2, 6]	Spectral index
	Inclusion rate	60%	50%	Fraction of pulsars with red noise
SGWB	A_{SGWB}	2.4×10^{-15}	–	Characteristic strain at $f_{\text{ref}} = 1/\text{yr}$
	γ_{SGWB}	13/3	–	Spectral index

A well-known parametrization of $\Omega_{\text{GW}}(f)$ is adopted by a scaling behavior as [62, and references therein]:

$$\Omega_{\text{GW}}(f) = \Omega_{\text{GW}}(f_{\text{ref}}) \left(\frac{f}{f_{\text{ref}}} \right)^\alpha \quad (7)$$

in which, the f_{ref} and α are a reference frequency and the spectral index of the signal, respectively. Various theoretical models predict different values for α with appropriate frequency domains [62]. For coalescing black hole binaries, we have $\alpha = \frac{2}{3}$. The $\alpha = -\frac{2}{3}$ and $\alpha = 0$ are associated with cosmic strings and primordial GWs from the Big Bang.

What we are observing from PTA in the presence of SGWB is a modification in the rotational frequency of the pulsar ν . For a given pulsar, the relative shift in the frequency is given by [17]:

$$\delta\nu \equiv \frac{\Delta\nu}{\nu} = -\frac{1}{2} \int_{t_{em}}^{t_{obs}} dt' \dot{h}_{ij}(t', \mathbf{x}_0(t')) n_i n_j \quad (8)$$

where t_{em} and t_{obs} are the emission and observation time of the pulse, respectively. The $\hat{\mathbf{n}}$ is the unit vector from earth to pulsar direction. The position of the pulsar at time t is $\mathbf{x}_0(t)$. The PTR of a th pulsar located at $\hat{\mathbf{n}}_a$ due to GWs is given by:

$$PTR^{(a)}(t, \hat{\mathbf{n}}_a) = \int_0^t dt' \delta\nu(t', \hat{\mathbf{n}}_a) \quad (9)$$

The spatial cross-correlation function of timing residuals affected by statistical isotropic SGWB and stationary regime reads as:

$$\mathcal{C}(\zeta, \tau) = \left\langle \frac{1}{T_{\text{span}}} \int dt PTR^{(a)}(t, \hat{\mathbf{n}}_a) PTR^{(b)}(t + \tau, \hat{\mathbf{n}}_b) \right\rangle_{\text{pairs}} \quad (10)$$

where T_{span} is the total observation duration, $\langle \rangle_{\text{pairs}}$ means the average on all available pulsar pairs separated by $\cos(\zeta) \equiv |\hat{\mathbf{n}}_a \cdot \hat{\mathbf{n}}_b|$. In the presence of an isotropic SGWB, we have also $\mathcal{C}(\zeta, \tau = 0) \sim \Gamma_{\text{HD}}(\zeta)$ and $\Gamma_{\text{HD}}(\zeta)$

indicates the smoking gun of SGWB and is given by the Hellings & Downs (HD) formula [157]:

$$\Gamma_{\text{HD}}(\zeta) = \frac{3}{2} \psi \ln(\psi) - \frac{\psi}{4} + \frac{1}{2} + \frac{1}{2} \delta_{ab} \quad (11)$$

and $\psi \equiv [1 - \cos(\zeta)]/2$.

III. DATA DESCRIPTION

In this section, we will describe theoretical models for generating SGWB signals on the PTA data. We will clarify the various components of timing residuals in synthetic PTA to examine the behavior of summary statistics extracted from graph-based analysis as an indicator of the SGWB. Furthermore, we will discuss observed PTAs to assess the detection capability and compare them with the established pipeline currently used by the international PTAs groups.

A. Synthetic PTA Data for SGWB

To evaluate the detection capability of our graph-based pipeline, we simulate mock PTA data incorporating the HD spatial correlation signature with simulation settings summarized in Table I. Our approach requires exact spatial correlations to validate topological detection criteria. The pulsar timing residuals (PTRs) obtained after fitting a timing model (TM) to the times of arrival (TOAs) contain multiple stochastic components:

$$PTR^{(a)}(t) = N_{\text{wn}}^{(a)}(t) + N_{\text{rn}}^{(a)}(t) + S_{\text{SGWB}}^{(a)}(t) \quad (12)$$

here, $N_{\text{wn}}^{(a)}(t)$ and $N_{\text{rn}}^{(a)}(t)$ are the white measurement noise and intrinsic red noise, respectively, and $S_{\text{SGWB}}^{(a)}(t)$ is the stochastic gravitational wave background signal, which is common to all pulsars but exhibits a spatially correlated angular structure (HD). We assume an idealized timing model fit, neglecting any TM uncertainties.

We distribute the pulsars uniformly across the sky to avoid biases in angular correlation measurements. The

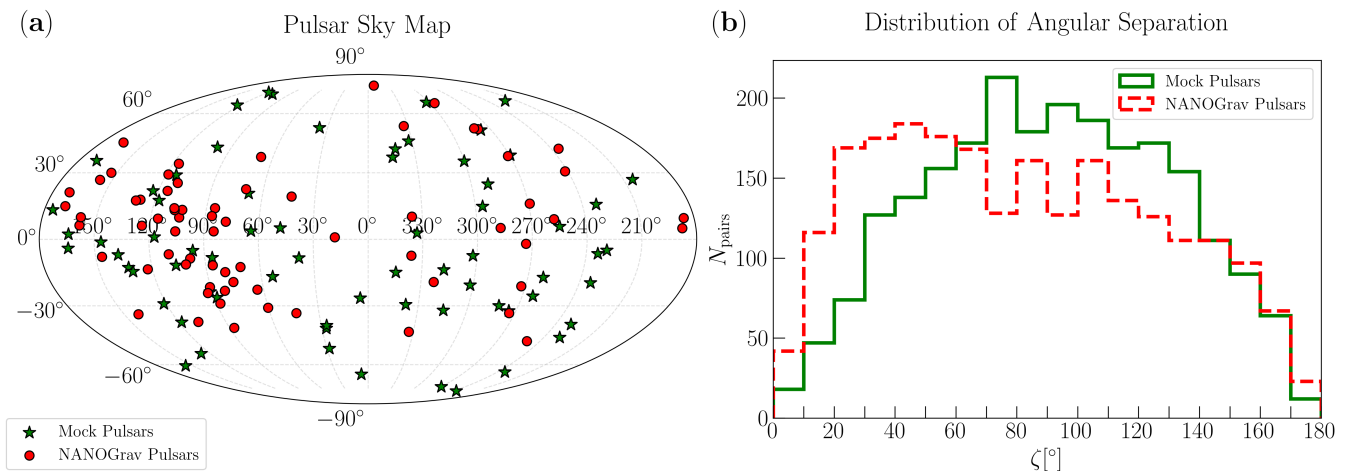


FIG. 2: (a) Sky distribution of mock PTA pulsars (green stars) and NANOGrav pulsars (red circles) in celestial coordinates (Right Ascension, Declination). (b) Histogram of angular separations between all unique pulsar pairs of the mock PTA (green solid) and NANOGrav (red dashed).

left panel of Figure 2 shows a realization of this uniform distribution for our mock array of 68 pulsars (green stars). The green solid line in the right panel is the distribution of angular separations of mock pulsars. The distribution is notably non-uniform where relatively fewer pulsar pairs are separated by very small (e.g., $< 20^\circ$) or very large separations (e.g., $> 160^\circ$), while most lie within intermediate angular ranges. As a result, the number of pulsar pairs contributing to the lowest and highest angular bins is limited, which can lead to increased statistical uncertainty in those regions.

Each pulsar's time series spans 15 years of *PTRs*, sampled uniformly at a 14-day cadence without any observational gaps or irregularities²¹. To construct the residuals, we first generate individual noise components, white measurement noise and intrinsic red noise, then inject the SGWB signal into the combined noises. The white noise component is modeled as uncorrelated Gaussian fluctuations with a fixed variance for each pulsar:

$$\langle N_{\text{wn}}^{(a)}(t)N_{\text{wn}}^{(b)}(t') \rangle = (\sigma^{(a)})^2 \delta(t - t') \delta_{ab} \quad (13)$$

where $(\sigma^{(a)})^2$ represents the noise strength for pulsar a , $\delta(t - t')$ is the Dirac delta function in time, and δ_{ab} ensures no cross-pulsar correlations. The values of $\sigma^{(a)}$ are drawn uniformly from the range [100, 1000] ns (Table I). The red noise component is simulated as a stationary Gaussian process with a power-law power spectral den-

sity:

$$\langle N_{\text{rn}}^{(a)}(f)N_{\text{rn}}^{(b)}(f') \rangle = \frac{A_{\text{rn}}^{(a)2}}{12\pi^2} \left(\frac{f}{f_{\text{ref}}} \right)^{-\gamma_{\text{rn}}^{(a)}} f_{\text{ref}}^{-3} \delta(f - f') \delta_{ab} \quad (14)$$

where A_{rn}^a and γ_{rn}^a are the strain amplitude and spectral index for pulsar a , respectively, and $f_{\text{ref}} = 1/\text{yr}$ is the reference frequency. Red noise is included in 60% of randomly selected pulsars, approximating its observed prevalence in real PTAs. Parameters $\log A_{\text{rn}}^a$ and γ_{rn}^a are drawn uniformly from the ranges listed in Table I.

The isotropic, Gaussian SGWB induces a common signal in all pulsars within a PTA. While the SGWB generates timing residuals with identical power spectra across the array, its distinctive spatial correlations are encoded by the HD curve. The one-sided power spectral density of the SGWB-induced residuals is given by:

$$P_{\text{SGWB}}(f) = \frac{H_0^2}{8\pi^4 f^5} \Omega_{\text{GW}}(f) \quad (15)$$

where H_0 is the Hubble constant. The spectral shape of Ω_{GW} depends on the physical origin of the SGWB. For astrophysical sources, such as a population of inspiraling supermassive black hole binaries (SMBHBs), the energy density spectrum is modeled as (Eq. (7)):

$$\Omega_{\text{GW}}^{\text{SMBHB}}(f) = \frac{2\pi^2 f^2}{3H_0^2} A_{\text{SGWB}}^2 \left(\frac{f}{f_{\text{ref}}} \right)^{3-\gamma_{\text{SGWB}}} \quad (16)$$

where A_{SGWB} is the characteristic strain amplitude of circular binaries evolving under gravitational radiation. The fiducial values of A_{SGWB} and γ_{SGWB} are listed in Table I.

Figure 3(a) displays simulated *PTRs* for three representative pulsars, comparing noise-only and SGWB + noise cases. The Fourier transformation of pulsar timing

²¹ Dealing with irregular sampled data can be accomplished through various methods. A prominent approach for creating equidistant sampling values involves convolving with a window function. This issue has been investigated in detail in [155].

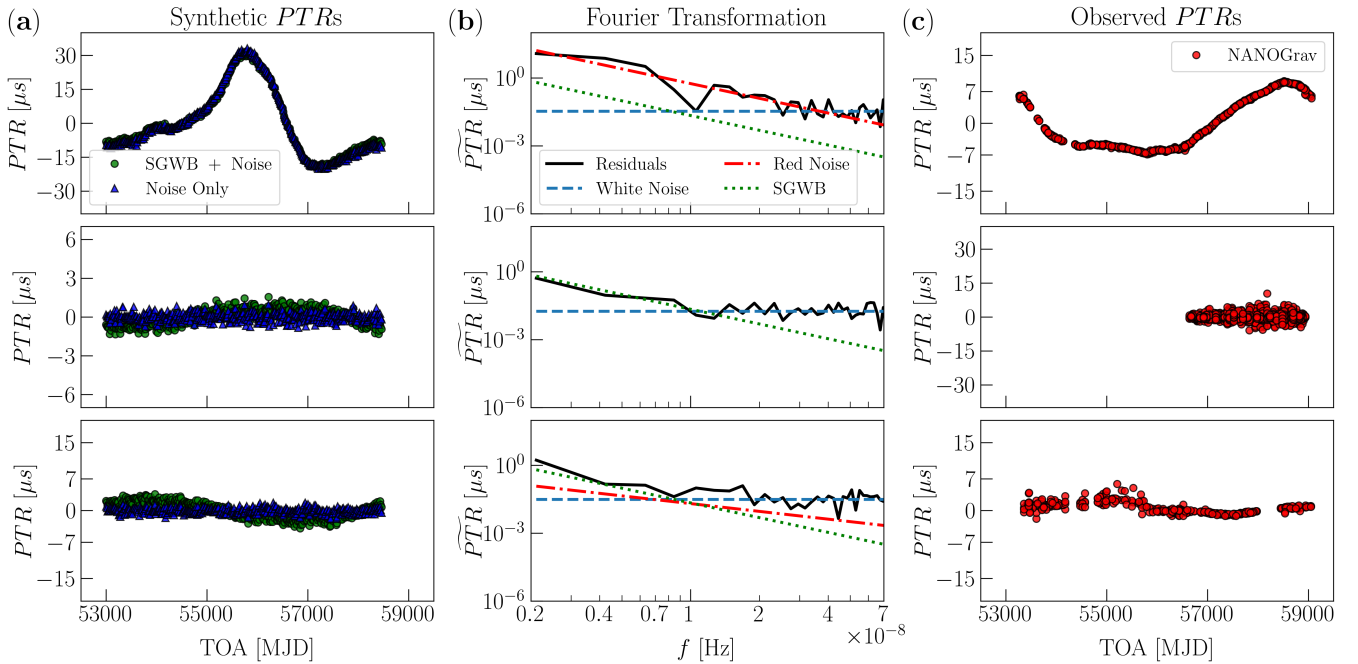


FIG. 3: (a) Simulated residuals for three representative pulsars showing noise-only (blue triangles) and SGWB+noise (green circles) cases. (b) Fourier transformation of mock data (black solid) with contributions from white noise (blue dashed), red noise (red dash-dotted), and SGWB signal (green dotted). The SGWB signal overlaps with red noise at low frequencies ($f \lesssim 1/\text{yr}$), illustrating the challenge of detection through single pulsar analysis. (c) Observed timing residuals of selected NANOGrav pulsars (red circles).

residuals (\widetilde{PTRs}) is depicted in Figure 3(b). The first pulsar (upper panel) exhibit strong red noise component which dominates the PTR signal, while the second pulsar (middle panel) compromise of white noise and SGWB signal without any intrinsic red noise. This makes the slight effect of SGWB to be visible on the timing residuals at low frequency regime. The third pulsar (lower panel) has comparable SGWB and red noise. The SGWB signal is indistinguishable from intrinsic red noise in individual pulsars, emphasizing the necessity of cross-correlation analysis for detection.

As mentioned before the distinctive signature of an isotropic, Gaussian SGWB in PTAs is the HD spatial correlation (Eq. (11)). However, additional spatial patterns may arise from different physical processes such as system-wide clock errors resulting in constant monopole correlation pattern, $\Gamma_{\text{MO}}(\zeta) = 1$. Dipole pattern indicate uncertainties in the solar system ephemeris, $\Gamma_{\text{DI}}(\zeta) = \cos\zeta$. To complete our investigation, we also consider the case where all pulsars share a common uncorrelated red noise signal (CURN), $\Gamma_{\text{CURN}}(\zeta) = 0$ in absence of the SGWB. Figure 4 compares these patterns using simulated data, showing both idealized (pure signal) and realistic (signal + noise) scenarios.

The SGWB signal is generated through eigenvalue decomposition of the target correlation matrix, with details provided in Appendix A. This method ensures exact spatial correlations with flexible switching between different

correlation patterns.

B. Observed PTA Data

We implement our graph-based method on the NANOGrav 15-year dataset²² (NG15) [188]. This dataset comprises high-precision timing observations from 68 millisecond pulsars monitored between 2004 and 2020. The pulsars are monitored with cadences between 1 – 4 weeks using the Arecibo Observatory (AEO), the Green Bank Telescope (GBT), and the Very Large Array (VLA). The observed pulsars distribution across the sky is shown in Figure 2(a) with filled red circles and their angular separations histogram is illustrated in Figure 2(b) with dashed red line. The distribution shows some geometrical biases due to telescope sky coverage. The timing residuals contain multiple stochastic components: white noise from radiometer and jitter effects, red noise present in approximately 50% of pulsars attributed to spin irregularities or interstellar medium variations, and potential common processes induced by the SGWB. The white noise strengths range from ~ 50 ns for the most stable pulsars (e.g., PSR J1937+21) to $\sim 5 \mu\text{s}$ for more noisy

²² <https://nanograv.org/science/data>

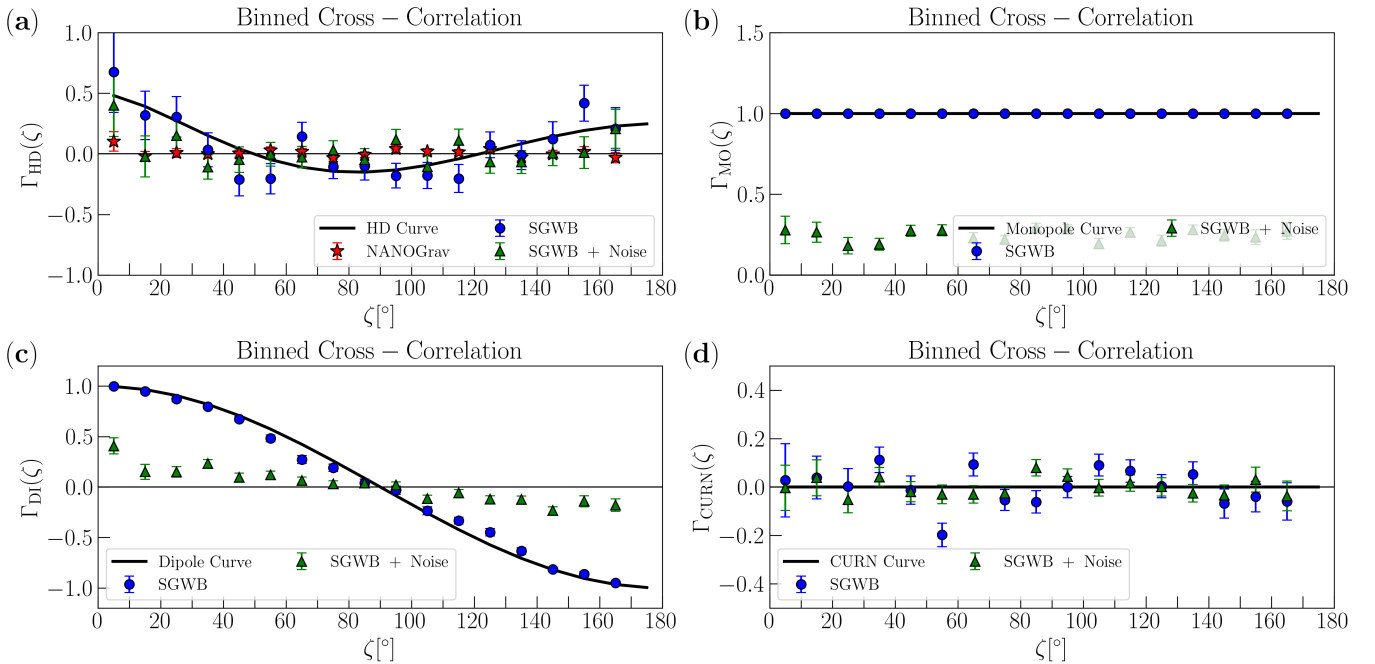


FIG. 4: Recovered angular correlation patterns for (a) Hellings & Downs (HD), (b) Monopole, (c) Dipole, and (d) CURN models. Blue circles show pure signal realizations, green triangles signal+noise, red stars NANOGrav observations, and black lines the theoretical correlation curves.

pulsars (e.g., PSR J0709+0458). Table I summarizes the observed data parameters and Figure 3(c) shows sample PTRs of the data. Unlike our idealized simulations, the NG15 dataset suffers from some data gaps, non-uniform data acquisition, TM and ephemeris uncertainties that may produce spurious spatial correlation patterns.

IV. IMPLEMENTATION OF GRAPH THEORY ON PTAS

The unique signature of an isotropic SGWB is the HD pattern which is encoded in the spatial correlation of the pulsar timing residuals. Traditional detection approaches, whether Bayesian or frequentist, rely on pre-modeling the SGWB's power spectral density and noise components, which make them sensitive to parameter priors and simplification assumptions, (e.g., Gaussianity and stationarity).

In this work, we propose a data-driven approach where the PTA pulsars are represented as a structured graph in the framework of graph theory. Constructing a graph from a single time-series is well established and there are various methods to accomplish this, e.g. *proximity graph*, *cycle graph*, *visibility graph*, *recurrence graph* and *transition graph* (see e.g. [176] and references therein). To establish a graph from multi-variable time series (Eq. (1)), two methods were introduced, the visibility graph [170] and correlation network [176]. A graph is denoted by $G = (V, E, \omega)$ in which $V \equiv \{v_a\}_{a=1}^{N_{PTA}}$ is the vertex

(node) set, $E = V \times V \equiv \{\epsilon_{ab} = (v_a, v_b) | v_a, v_b \in V\}_{a,b=1}^{N_{PTA}}$ is the edge (link) set and weight function is defined as $\omega : E \rightarrow \mathbb{R}$. The degree of a node, v_a , is the number of nodes straightly connected with a th node by non-zero weight, $k_a \equiv \sum_b (1 - \delta_{0, \omega_{ab}})$. To investigate the correlation pattern between the pulsars, we use the correlation network approach where the graph nodes represent the pulsars and their mutual cross-correlation determine the weight function, ω . The HD correlation signature is naturally encoded in the graph and by analyzing the global and local properties of the graph we expect to trace the footprint of SGWB in the PTA data from different perspective.

A. Complex Network Construction from PTA Data

Figure 5 illustrates the pipeline used to construct a graph from PTA data. Starting from the PTRs of the pulsars, we compute pairwise cross-correlations, $\mathcal{C}(\zeta, \tau = 0) = \langle PTR^{(a)}(t), PTR^{(b)}(t) \rangle_t$, and the corresponding angular separations, ζ^{ab} , between pulsar pairs. A weighted and undirected graph, $G(V, E, \omega)$, is then constructed by applying an angular separation threshold, $\bar{\zeta}$, such that, if $\zeta^{ab} < \bar{\zeta}$, an edge is added between pulsars a and b with weight equal to their cross-correlation; otherwise, no edge is added. However, we exclude the angular ranges between $[39.5^\circ - 63^\circ]$ and $[104^\circ - 137.5^\circ]$ where the absolute value HD-curve are less than 0.1 and it resembles a noise-like fluctuations. This strategy leads

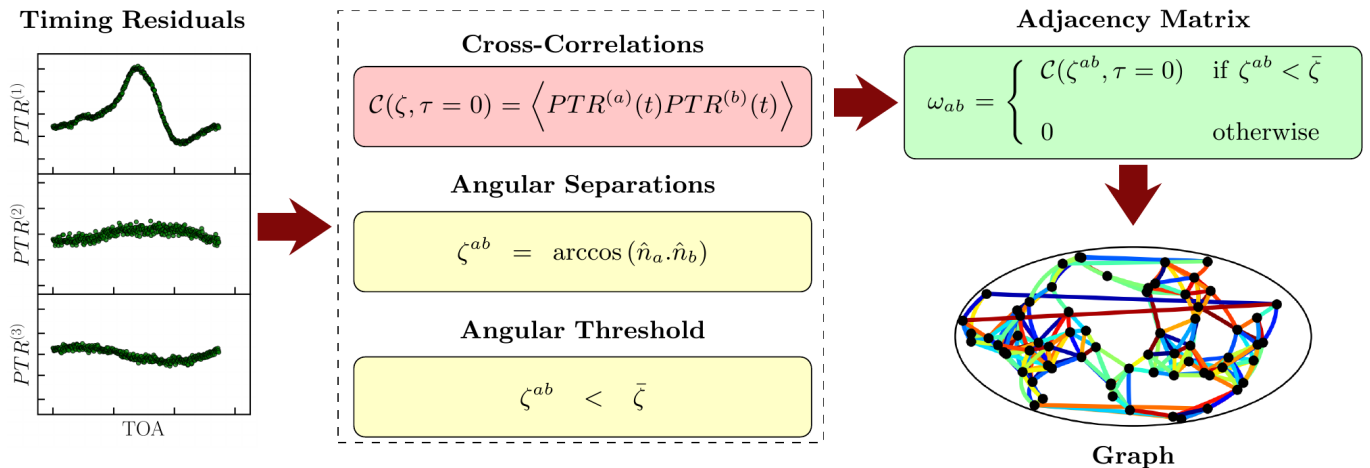


FIG. 5: The pipeline for constructing a weighted correlation network from PTA data. Nodes represent pulsars, pulsar pairs that have angular separation below a chosen threshold, $\bar{\zeta}$, will be connected, and edge weights correspond to the cross-correlations of timing residuals, resulting in the adjacency matrix that defines the graph $G(V, E, \omega)$.

to lose almost 41% of total pulsar pair connections. It is worth mentioning that in our approach, the edge weight may have negative value depending on the corresponding angular separation, ζ^{ab} .

To study how the spatial correlation structure evolves, we construct a family of graphs by systematically varying the angular separation threshold, $\bar{\zeta}$, between 0° and 180° . A sample of resulting graphs is shown in Figure 6. For small thresholds (e.g., $\bar{\zeta} = 30^\circ$), the graph is sparsely connected, capturing only the correlations between nearby pulsar pairs. As $\bar{\zeta}$ increases, more distant pairs are added, leading to a denser graph, until the threshold reaches 180° , the graph contains the maximum number of allowed connections. This $\bar{\zeta}$ procedure is applied to explore the evolution of PTA correlation graph properties with the angular scales.

B. Imprint of SGWB on the Graph-based summary statistics of PTAs

The geometrical and topological of a typical network are encoded in several quantities such as the *Probability distribution for degree* of all nodes in a network, $p(k) = \frac{1}{N} \sum_{a=1}^{N_{\text{PTA}}} \delta_{k, k_a}$, *Graph cumulants*, *Degree centrality* - indicating the importance of a th node, $k_a/(N_{\text{PTA}} - 1)$, *Betweenness centrality* - the number of shortest paths between any pairs of nodes going through a distinct node, *Closeness centrality* - the average of shortest path between a given node and all other nodes, *eigenvector centrality* - a quantification of influence of a given node, *Transitivity* - representing the density of possible triangles (three nodes connected together) in the constructed network, *Average clustering coefficient*, *Average node strength*, *assortativity*, etc. [189–193].

To quantify the structural signatures of an SGWB in correlation graphs constructed from PTA data, we com-

pute a set of five graph theory metrics outlined below, which we anticipate to be almost sensitive to topological properties of the complex network [189–192]. The reason for choosing such measures is their ability to capture the SGWB fingerprint encoded in the graph weight function, ω . However, we have also evaluated various geometric characteristics of the graph (such as centrality measures, node degree statistics), and our results reveal that they do not have adequate sensitivity to identify GW.

- **I) Average clustering coefficient:** This quantity measures the tendency of nodes (pulsars) to form tightly connected triangles. A higher value indicates locally clustered groups with strong correlations, consistent with the spatial structure from an SGWB. The weighted clustering coefficient for node a is

$$C_a(\bar{\zeta}) = \frac{1}{k_a(k_a - 1)} \sum_{b \neq d \neq a} (\hat{\omega}_{ab} \hat{\omega}_{ad} \hat{\omega}_{bd})^{1/3} \quad (17)$$

where k_a its degree and $\hat{\omega}_{ab}$ is the edge weight between node a and b normalized by the largest weight in the graph. Accordingly, the global average is:

$$C_\omega(\bar{\zeta}) \equiv \langle C_a(\bar{\zeta}) \rangle_a = \frac{1}{|V|} \sum_a C_a(\bar{\zeta}) \quad (18)$$

- **II) Average node strength:** The node strength s_a is the sum of all edge weights connected to the a th node:

$$s_a(\bar{\zeta}) = \sum_{b \neq a} \omega_{ab} \quad (19)$$

The mean of all individual node strengths within the graph which reflects overall pulsars correlation

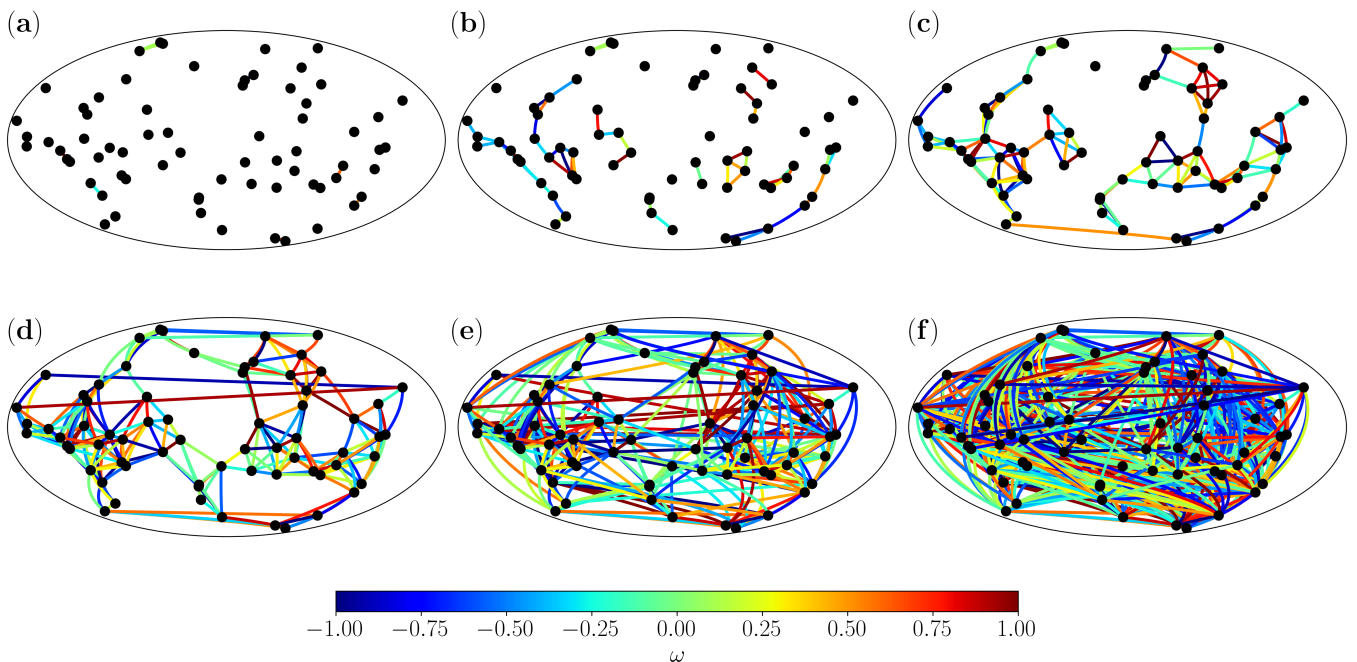


FIG. 6: Correlation graphs constructed from mock PTA data for different angular thresholds: (a) 10° , (b) 20° , (c) 30° , (d) 50° , (e) 70° , and 90° . Nodes (filled black circles) represent pulsars.

strength:

$$s_\omega(\bar{\zeta}) \equiv \langle s_a(\bar{\zeta}) \rangle_a = \frac{1}{|V|} \sum_{a=1}^{N_{\text{PTA}}} \sum_{b>a} \omega_{ab}. \quad (20)$$

Higher values indicates pervasive correlations in the data which is useful for discriminating the signal from pure noise.

- **III) Generalized assortativity coefficient:** This feature examine whether strongly correlated pulsars connect to other strongly correlated pulsars:

$$r_\omega(\bar{\zeta}) \equiv \frac{\sum_{b>a} [s_a(\bar{\zeta}) - s_\omega(\bar{\zeta})][s_b(\bar{\zeta}) - s_\omega(\bar{\zeta})]}{\sum_a [s_a(\bar{\zeta}) - s_\omega(\bar{\zeta})]^2}. \quad (21)$$

The positive value suggests hub formation whereas the negative value indicates mixing state. The common definition of assortativity is based on nodes degree, whereas its generalized definition for weighted graph relies on the node strength [194].

- **IV) Mean edge weight:** This is the first graph cumulant derived from probability distribution of edge weights and it reads as:

$$\mu_\omega(\bar{\zeta}) = \frac{1}{|E_{\bar{\zeta}}|} \sum_{a \neq b} \omega_{ab}. \quad (22)$$

This average pairwise cross-correlation is sensitive to signal.

- **V) Standard deviation of edge weight:** The second graph cumulant of edge weights, which is the fluctuation of edge weights, or in other words, the correlation variability, reads as:

$$\sigma_\omega(\bar{\zeta}) = \sqrt{\frac{1}{|E_{\bar{\zeta}}| - 1} \sum_{a \neq b} [\omega_{ab} - \mu_\omega(\bar{\zeta})]^2}. \quad (23)$$

Low values represent homogeneity, while higher values indicate somehow correlation anisotropies in the PTA.

Thus far, we introduced the graph-based summary statistics as: $\mathcal{G} : \{C_\omega, s_\omega, r_\omega, \mu_\omega, \sigma_\omega\}$ and in the following, we will look for the influence of various components in our synthetic PTA including noise as the Baseline and injected signal with various spatial correlation patterns (Γ_{HD} , Γ_{MO} , Γ_{DI} and Γ_{CURN} see subsection III A) on the summary statistics, \mathcal{G} . Our graph-based summary statistics has also angular separation threshold degree of freedom, hence, $\mathcal{G} : \{\mathcal{G}_\omega(\bar{\zeta}_i)\}$ and \diamond can be replaced by C, s, r, μ, σ . The i denotes the label of each bin, which ranges from 1 to 18, corresponding to $\bar{\zeta} \in [10^\circ, 180^\circ]$ with a bin size $\Delta\bar{\zeta} = 10^\circ$. Therefore \mathcal{G} has total of 90 elements.

Before computing the element of summary statistics and for the sake of clarity, we show the behavior of adjacency matrix for $N_{\text{PTA}} = 68$ of size 68×68 for various

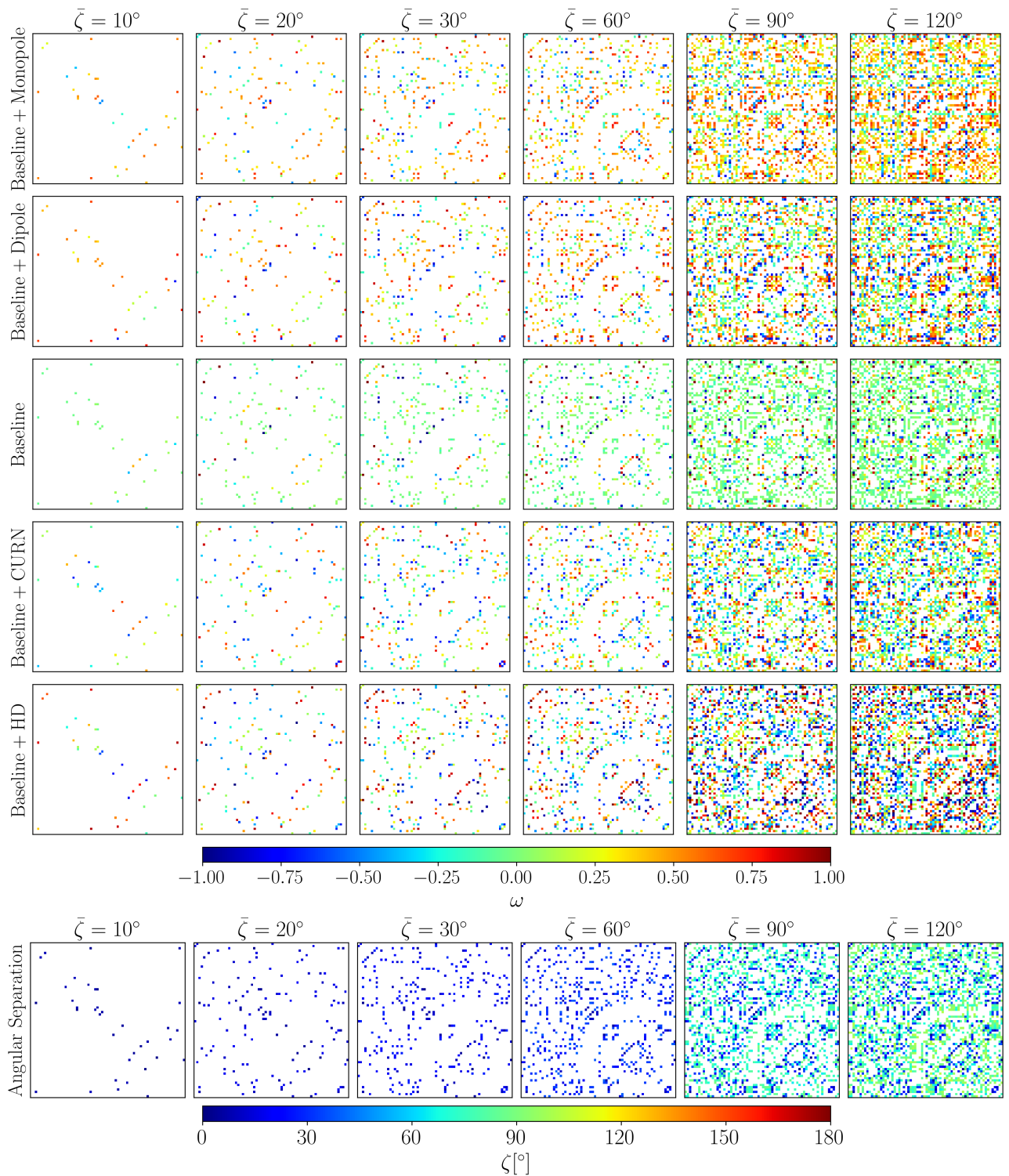


FIG. 7: The density plots for distinct components employed in the construction of graphs are shown for a range of angular separation values ($\bar{\zeta}$) from left to right. Each panel is a matrix of size 68. The first five rows depict the sample averaged of adjacency matrices, with elements denoted as ω_{ab} for various spatial correlation templates applied to the PTA network. The last row reveals the matrix whose elements consist of the values of ζ_{abs} for a particular threshold, $\bar{\zeta}$. The white pixels in the matrices are devoted to pairs that we have excluded and whose angular separations belong to the ranges between $[39.5^\circ - 63^\circ]$ and $[104^\circ - 137.5^\circ]$ (see subsection IV A for more details).

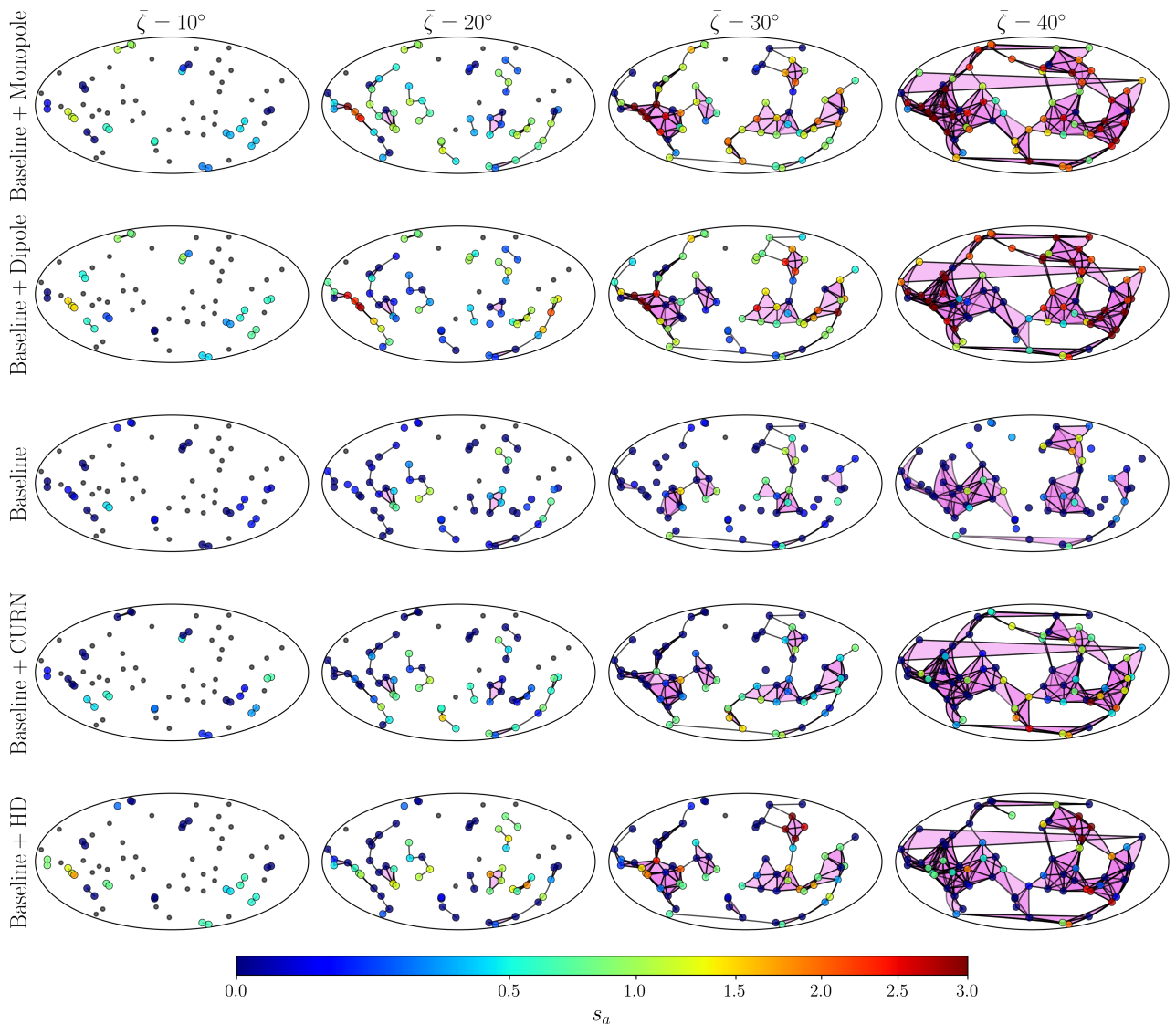


FIG. 8: The constructed graph from PTA data for a range of angular separation values ($\bar{\zeta}$) from left to right. Each row corresponds to a specific spatial correlation template identified as Baseline + Monopole, Baseline + Dipole, Baseline, Baseline + CURN, and Baseline + HD. The points are associated with graph nodes (pulsars), with different node colors reflecting their strength values (s_a). Two nodes have an edge if and only if their spatial angular separation satisfies the condition $\zeta_{ab} \leq \bar{\zeta}$. The abundance of triangles, which is almost quantified by the average clustering coefficient up to a geometrical mean value (Eq. (18)), is evidently insufficient for the noise template.

values of $\bar{\zeta}$ in the upper part of Figure 7. The associated overall amount of edges for constructed graph is also indicated in the last row of Figure 7. The first five rows in the Figure 7 correspond to a realization of adjacency matrices for Baseline + Monopole, Baseline + Dipole, Baseline, Baseline + CURN and Baseline + HD templates exerted on the PTA, respectively. The last row depicts that the higher value of $\bar{\zeta}$, the more dense graph is. The white pixels in these plots figures out the pairs that we have masked to reduce the spurious impact of noise (see subsection IV A). The angular separation values for masked pairs are in the ranges between $[39.5^\circ - 63^\circ]$ and $[104^\circ - 137.5^\circ]$. This achievement is consistent with the

graphs illustrated in Figure 6.

To give a more complete view concerning the graph-based summary statistics, we depict the constructed graph in Figure 8. Assuming a specific spatial correlation template, the overall properties of the graph vary. Each row corresponds to a specific spatial correlation template identified as Baseline + Monopole, Baseline + Dipole, Baseline, Baseline + CURN, and Baseline + HD. The points are associated with graph nodes (pulsars), with different nodes' colors reflecting their strength values (s_a). Two nodes have an edge if and only if their spatial angular separation satisfies the condition $\zeta_{ab} \leq \bar{\zeta}$. An obvious change for different templates, which is visually

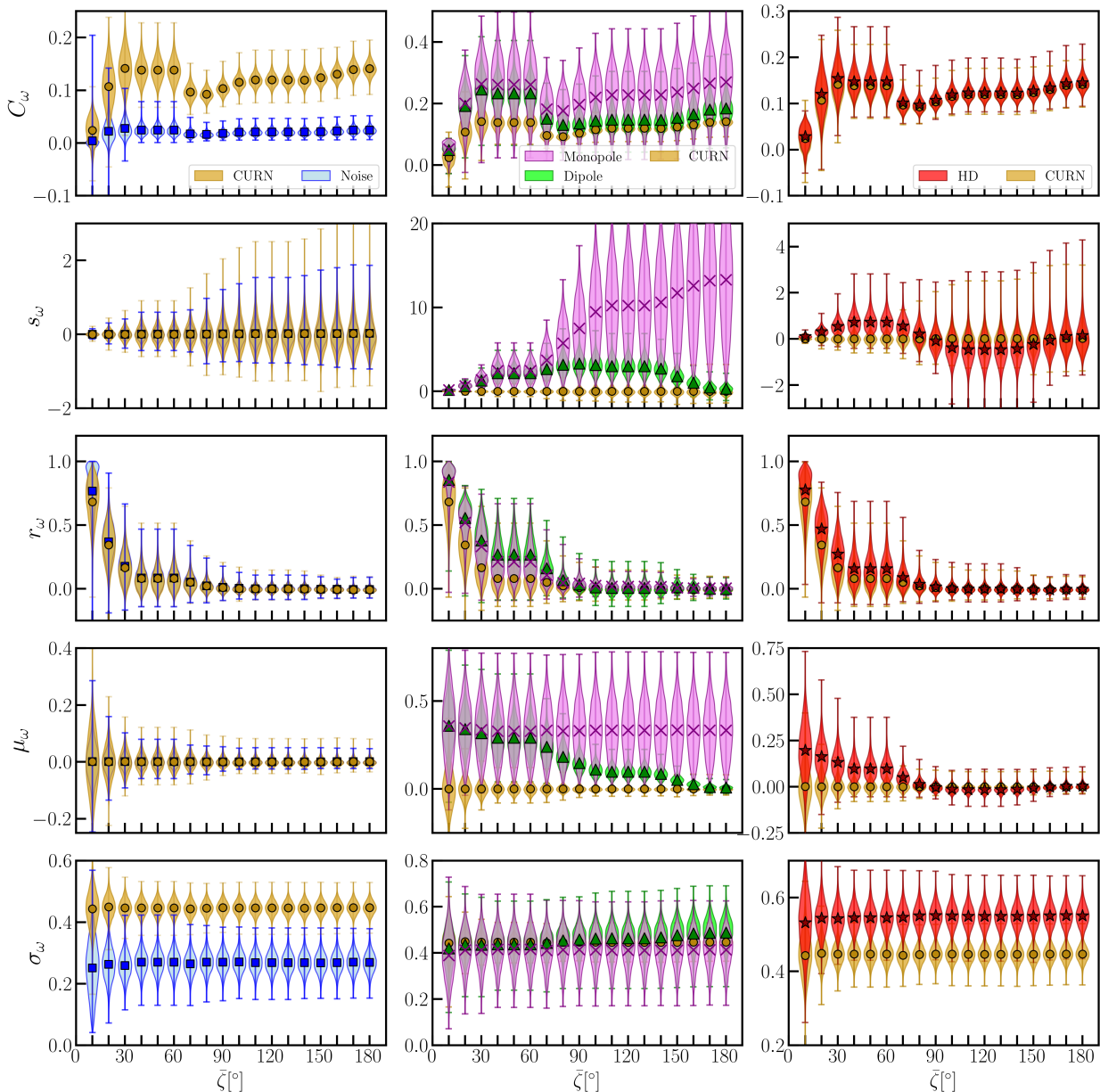


FIG. 9: The empirical distributions of graph measures across angular thresholds for 10000 realizations. The graph measures are from top to bottom: I) Average clustering coefficient, II) Average node strength, III) Generalized assortativity coefficient, IV) Mean edge weight, and V) Standard deviation of edge weight. Left column compares the Baseline + CURN (gold violins) with Baseline (blue violins) distributions. Comparison of Baseline + Monopole (violet violins) and Baseline + Dipole (green violins) with Baseline + CURN are depicted in the middle column. Last column shows the comparison between Baseline + HD (red violins) and Baseline + CURN.

captured, is the abundance of triangles. This statistic is quantified by the average clustering coefficient up to the geometrical mean value (Eqs. (17) and (18)). As expected from the clustering feature, the number of triangles for the Baseline is less than the other spatial templates. It is worth noting that the triangles, \triangle_{abd} , with a geometrical mean, $(\omega_{ab}\omega_{ad}\omega_{bd})^{1/3}$, less than 0.1 have

been removed for better visualization.

Figure 9 shows the empirical distributions of graph-based summary statistics computed over 10,000 realizations of synthetic data with fiducial parameter values listed in Table I for different spatial correlation models as a function of angular separation thresholds.

The first row of Figure 9 displays the first element of

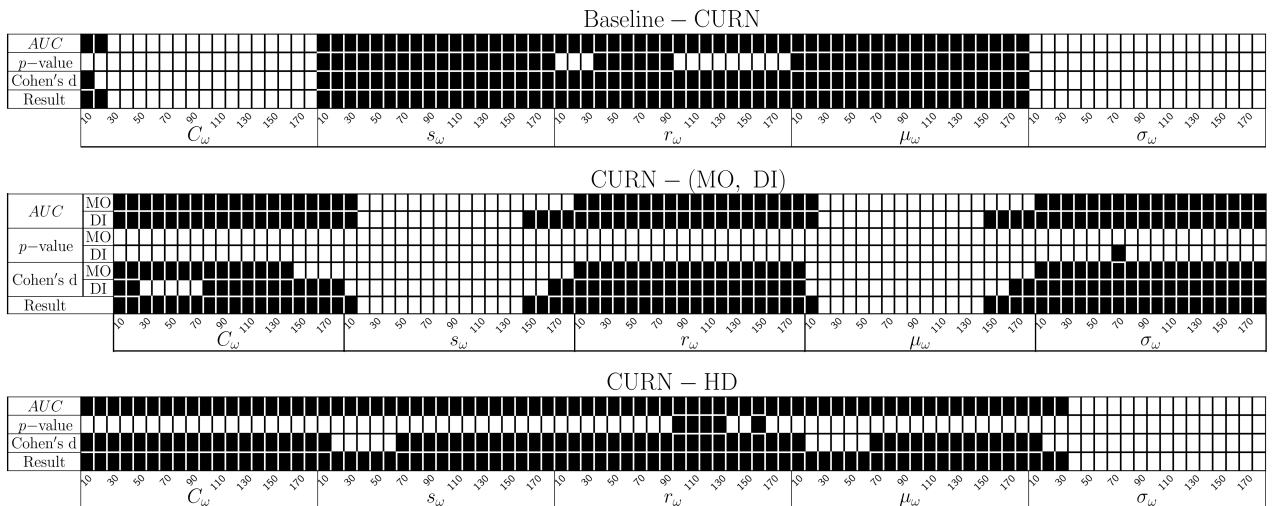


FIG. 10: The binary representation of 90-component summary statistics responses to conditions assumed by evaluation metrics, such as AUC , p -value, and Cohen's d . The white pixel refers to a component that accepts the condition associated with each metric, while the black pixel signifies a rejection of the condition. The pixels for the result row are white if all conditions imposed by the evaluation metrics are satisfied.

graph-based summary statistics, C_ω , as a function of $\bar{\zeta}$ (Eq. (18)). This criterion quantifies the nature of 3-point statistics (Δ_{abd}). The presence of common signal, CURN ($\Gamma_{\text{CURN}} = 0$), produces more triangles resulting in higher average clustering coefficient (filled circle symbols in the left panel of first row). It turns out that for only Baseline, we expect to have uncorrelated behavior for ω_{ab} as justified by the third row of Figure 7 resulting in negligible average clustering coefficient (filled blue square symbols). The middle panel of first row in Figure 9 compares the C_ω for non-HD, namely monopole and dipole with CURN template. This panel demonstrates that the Baseline + Monopole possesses higher clustering coefficient for wide range of angular separation thresholds (cross symbols). Whereas the Baseline + Dipole has excess triangles just for almost $\bar{\zeta} \lesssim 60^\circ$ (filled green triangle symbols). The dipole spatial pattern ($\Gamma_{\text{DI}} = \cos(\bar{\zeta})$) has $\bar{\zeta}$ -dependency and therefore, the difference between its edge weights and that of monopole spatial pattern ($\Gamma_{\text{MO}} = 1$) becomes considerable as $\bar{\zeta}$ increases. This behavior can be seen by comparing the evolution of edge weights as indicated in the first and second rows of Figure 7. Incorporating the SGWB, whose characteristics is given in Table I, the values of elements of the adjacency matrix and their corresponding evolution concerning $\bar{\zeta}$ is illustrated in the fifth row of Figure 7. Accordingly, the value of C_ω (filled red star symbols) achieves a similar values with correspondence of Baseline + CURN. Our results confirm that the average clustering coefficient is almost unable to distinguish the imprint of Baseline + HD and Baseline + CURN.

The second row of Figure 9 reveals the sample distribution of average strength (Eq. (20)) for various templates. Obviously, this measure equates to a summa-

tion on all lower triangle portions of the adjacency matrix, represented by $\langle s_a \rangle_a$. Figure 8 shows that the values of s_a for the monopole and dipole templates are statistically higher than the corresponding values for the Baseline, Baseline + CURN, and Baseline + HD. We show the distribution function of s_ω for the Baseline and Baseline + CURN in the left panel of the second row of Figure 9. This result confirms that average strength is not a proper measure for signal detection. From the middle panel of the second row of the mentioned figure, s_ω is capable of detecting non-HD properly. The HD detection through the average strength is statistically weak (right panel of the second row of Figure 9).

The generalized assortativity coefficient, r_ω as a function of $\bar{\zeta}$ is depicted in the third row of Figure 9. For all range of $\bar{\zeta}$ and for all templates considered in this research, the mean value of r_ω is positive and by increasing the angular separation, the generalized assortativity coefficient tends to zero. The measure r_ω , quantifies the similarity in node strength within the graph. For small angular separations, graph sparsity restricts the variability in the strength of each node, which is related to the cumulative edge weights of a given node. Therefore, it in turn elevates the r_ω metric. This behavior is also realized from the value of s_a displayed by the color-bar in Figure 8. Our results indicate that r_ω is neither sufficiently sensitive for signal detection nor effective for discriminating non-HD correlations. From the right panel of third row of Figure 9, we obtain that the $r_\omega^{\text{Baseline+HD}} \gtrsim r_\omega^{\text{Baseline+CURN}}$ for $\bar{\zeta} \lesssim 80^\circ$.

The fourth member of graph-based summary statistics which is associated with mean edge weight (Eq. (22)) is depicted as function of $\bar{\zeta}$ in the fourth row of Figure 9. The ensemble average of μ_ω for Baseline is

clearly zero which is similar to Baseline – CURN template. The mean edge weight for Baseline – Monopole becomes constant, while the angular separation dependency is achieved for Baseline – Dipole model. According to middle panel of forth row of mentioned figure, the mean edge weight is capable for non – HD detection. The mean edge weight μ_ω for Baseline + HD is positive at small angular scales but asymptotically approaches zero as $\bar{\zeta}$ increases, due to compensation from negative edge weights. Consequently, μ_ω becomes an ineffective measure for detecting SGWB. Figure 7 shows that the mean ω_{ab} values for the Baseline + Monopole and Baseline + Dipole templates are higher than those for the Baseline, Baseline + CURN, and Baseline + HD templates.

The final graph-based measure, the edge weight

standard deviation (σ_ω), is significantly higher for Baseline + CURN than for Baseline. This makes it a crucial statistic for common signal detection. The ensemble average of σ_ω for Baseline + HD with characteristics reported in Table I gets the highest values compared to the rest of the templates. A comparison of details between Baseline + CURN and Baseline + HD confirms that a significant difference exists for all ranges of angular separation (the right panel of the last row of Figure 9). The diversity in ω_{ab} , quantified by σ_ω , is realized in the first five rows of Figure 7. This is particularly evident when comparing the fourth and fifth rows, which show that $\sigma_\omega^{\text{Baseline+HD}} \gtrsim \sigma_\omega^{\text{Baseline+CURN}}$ for all values of $\bar{\zeta}$.

To quantify the discriminative capability of our graph-based summary statistics, we compare the following three pairs:

$$(x_{\text{null}}, x_{\text{signal}}) \in \{(\text{Baseline}, \text{Baseline} + \text{CURN}), (\text{Baseline} + \text{CURN}, \text{Baseline} + \text{non} - \text{HD}), (\text{Baseline} + \text{CURN}, \text{Baseline} + \text{HD})\},$$

through the following three metrics:

a) Area under the receiver operator characteristic (ROC) curve (AUC) defined as the probability that a signal value (x_{signal}) exceeds a null value (x_{null}), $AUC = P(x_{\text{signal}} > x_{\text{null}})$ [195];

b) Welch's t -test p -value indicates a significant difference between the means of the signal and null distributions [196];

c) Cohen's d which quantifies the standardized effect size between distributions [197].

To adopt a more conservative approach, we assume that a feature is regarded as a *detection indicator* if it satisfies all the subsequent criteria:

$$AUC_\diamond \geq 0.99, \quad p_\diamond\text{-value} \leq 0.0027, \quad \text{and} \quad \text{Cohen's } d_\diamond \geq 2 \quad (24)$$

where \diamond can be replaced by element of \mathcal{G} . The aforementioned criteria ensure excellent separability, high significant ($\gtrsim 3\sigma$) and large difference between the means of signal and null distributions.

Throughout this paper for convenience, we use following abbreviations for signal-null pairs:

$$\begin{aligned} \text{Baseline} - \text{CURN} &\equiv (\text{Baseline}, \text{Baseline} + \text{CURN}), \\ \text{Baseline} - (\text{MO}, \text{DI}) &\equiv (\text{Baseline} + \text{CURN}, \text{Baseline} + \text{non} - \text{HD}) \quad \text{and} \\ \text{CURN} - \text{HD} &\equiv (\text{Baseline} + \text{CURN}, \text{Baseline} + \text{HD}) \\ &(\text{Baseline} + \text{CURN}, \text{Baseline} + \text{HD}). \end{aligned}$$

For common signal detection, Baseline – CURN, we examine all 90-component summary statistics, \mathcal{G} . Figure 10 indicates the behavior of each element of \mathcal{G} taking into account AUC , p -value, and Cohen's d evaluation metrics in the binary style. The white and black boxes are denoted to accept and reject metric conditions (Eq. (24)), respectively. The result row is white if and only

if all metrics meet the conditions. For common signal detection the C_ω and σ_ω are almost proper measures. This is also consistent with the results indicated in the first and last left panels of Figure 9. For the non – HD scenario, the s_ω and μ_ω are more suitable, as confirmed by the middle panels in the second and third rows of Figure 9. The only measure that performs well for SGWB detection is σ_ω . This accomplishment is validated by the lower right panel of Figure 9.

Now, according to the results from the upper panel of Figure 10 (Baseline – CURN), we define the merit feature vector for common signal detection as: $\mathbf{V}_{\text{detection}} : \{\mathcal{G}_{\text{merit}}\}$. The $\mathcal{G}_{\text{merit}}$ consists of a subset of members from \mathcal{G} that fulfill all metric conditions (Eq. (24)). Having the $\mathbf{V}_{\text{detection}} : \{C_\omega, \sigma_\omega\}$, we turn to dealing with unknown PTR data recorded in the observation for signal detection purpose. Through the computation of the components of $\mathbf{V}_{\text{detection}}$ for the observed data, from which the spatial correlation pattern has been eliminated through either phase shuffling or by randomizing the positions of pulsars in the sky, we make $\mathbf{V}_{\text{detection}}^{\text{data-shuf}}$. Furthermore, the C_ω and σ_ω are computed for the Baseline data sets, resulting in the determination of $\mathbf{V}_{\text{detection}}^{\text{Baseline}}$. To establish a quantitative threshold for declaring a common signal detection, we define a z -score for each component of the merit feature vector. This score, $z \equiv (\mathbf{V}_{\text{detection}}^{\text{data-shuf}} - \mathbf{V}_{\text{detection}}^{\text{Baseline}}) / \sigma_{\mathbf{V}_{\text{detection}}^{\text{Baseline}}}$ compares the merit feature vector values for the CURN like data set to the distribution of Baseline values. The components of $\mathbf{V}_{\text{detection}}$ with a z -score value exceeding a specified threshold are qualified for signal detection. We implement a voting system requiring the majority of elements of $\mathbf{V}_{\text{detection}}$ to be triggered to claim a common signal

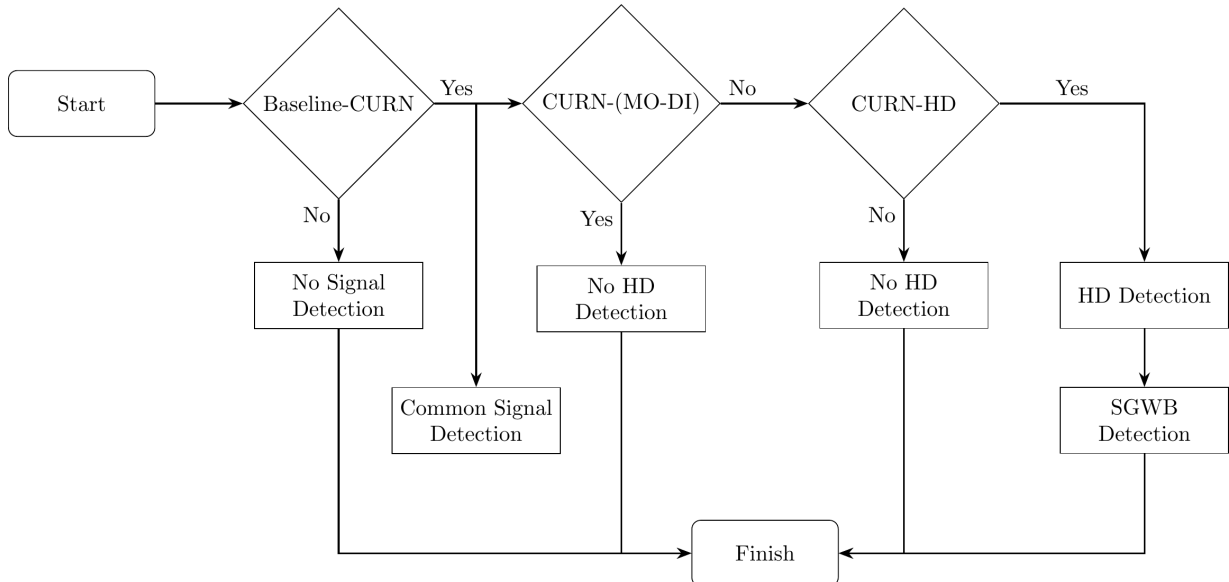


FIG. 11: Decision strategy for the SGWB detection pipeline. The sole pathway for a positive detection requires a positive result in Baseline – CURN, a negative result in CURN – (MO – DI), and a positive result in CURN – HD.

detection. This ensures that the false alarm probability (FAP) to be lower than 0.0027 , which is associated with the probability of triggering below the 3σ level of the multivariate distribution, with degree of freedom equivalent to the size of the merit feature vector. According to the implemented voting system, the criterion for which we are eventually allowed to announce a common signal siren, is defined by counting the number of elements in $\mathcal{V}_{\text{detection}}$ that have been triggered. This is only permissible if this number is equal to or greater than the minimum required number of elements in $\mathcal{V}_{\text{detection}}$, where this minimum number is determined by the predefined FAP value. The probability of triggering m elements from a total of n is approximately estimated by taking into account the probability of choosing the m elements from n , multiplied by the probability of the m elements being activated under the null hypothesis, with triggering threshold of 2.85σ allowing for faint signal detection. This condition results in approximately $\sim 65\%$ of the elements in the feature vector $\mathcal{V}_{\text{detection}}$ being activated for detection, corresponding to a credibility level of 3σ .

When a positive alert for common signal detection occurs, regardless of the spatial correlation pattern, it now becomes essential to examine the nature of the spatial correlation. Considering the prevalence of monopole and dipole patterns in the *PTRs* observations, this part of the observation pipeline should concentrate on studying the distinctions between the CURN and monopole as well as dipole patterns, which is called the non – HD scenario (CURN – (MO – DI)). The merit feature vector for the non – HD strategy is $\mathcal{V}_{\text{non-HD}} : \{s_\omega, \mu_\omega\}$ which has been obtained from the middle panel of Figure 10. In analogy to the common signal detection approach, we compute $z \equiv (\mathcal{V}_{\text{non-HD}}^{\text{data}} - \mathcal{V}_{\text{non-HD}}^{\text{data-shuf}}) / \sigma_{\mathcal{V}_{\text{non-HD}}^{\text{data-shuf}}}$. When at

least 65% of the components of $\mathcal{V}_{\text{non-HD}}$ have a z value exceeding 2.85 , the outcome of CURN – (MO – DI) discrimination reveals a pattern resembling either monopole or dipole in the observed data. If our criteria indicate the presence of a monopole or dipole in the data, any subsequent search for a HD pattern is meaningless. This conclusion is justified by examining the behavior of s_ω and μ_ω (Figure 9) for the CURN and HD models which is demonstrating similarity between two spatial patterns. Therefore, any significant detection of a monopole or dipole essentially indicates a higher significance for non – HD patterns. This, in turn, conservatively rules out the presence of a SGWB.

If the monopole and dipole patterns are ruled out, the analysis should subsequently proceed to the HD search (CURN – HD). The merit feature vector utilized for SGWB detection is denoted as $\mathcal{V}_{\text{HD}} : \{\sigma_\omega\}$, as depicted in the lower panel of Figure 10. We then compute $z \equiv (\mathcal{V}_{\text{HD}}^{\text{data}} - \mathcal{V}_{\text{HD}}^{\text{data-shuf}}) / \sigma_{\mathcal{V}_{\text{HD}}^{\text{data-shuf}}}$. Validation of the SGWB detection requires that at least 65% of the components in \mathcal{V}_{HD} have a $z \geq 2.85$, corresponding to a 3σ credibility level.

Figure 11 outlines our proposed strategy for SGWB detection according to the graph-based analysis. A conservative HD detection is only claimed following a positive Baseline – CURN result, a negative CURN – (MO – DI) result, and finally, a significant CURN – HD difference.

C. Scaling effects on graph-based detection

To evaluate the robustness and performance of our graph-based detection framework under varying observational and astrophysical conditions,

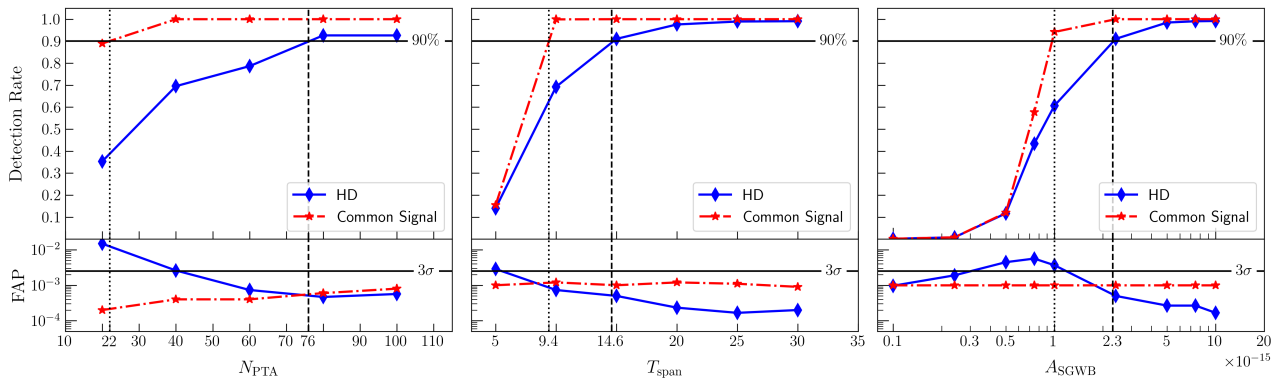


FIG. 12: Detection rate and false alarm probability (FAP) of the SGWB graph-based pipeline as a function of number of pulsars N_{PTA} (left panel), observing time span T_{span} (middle panel), and SGWB strain amplitude A_{SGWB} (right panel). The Blue solid lines show the SGWB detection, and the red dash-dotted line depicts the common signal detection. The vertical black dashed lines mark the thresholds where the detection rate for SGWB exceeds 90%, and the vertical black dotted lines show the thresholds for the common process.

$\{N_{\text{PTA}}, T_{\text{span}}, A_{\text{SGWB}}\}$, we conduct a systematic scalability study. Specifically, we generate 10,000 realizations for each configuration while independently varying three key parameters around their fiducial values given in Table I: $N_{\text{PTA}} = \{20, 40, 60, 80, 100\}$ pulsars, $T_{\text{span}} = \{5, 10, 15, 20, 25, 30\}$ years, and $A_{\text{SGWB}} = \{1.0 \times 10^{-16}, 2.5 \times 10^{-16}, 5.0 \times 10^{-16}, 7.5 \times 10^{-16}, 1.0 \times 10^{-15}, 2.4 \times 10^{-15}, 5.0 \times 10^{-15}, 7.5 \times 10^{-15}, 1.0 \times 10^{-14}\}$.

Detection performance is evaluated using the feature-based strategy described in subsection IV B. Figure 12 show the detection rate and the FAP of the pipeline with respect to N_{PTA} , T_{span} , and A_{SGWB} . The FAP of common signal (red dash-dotted line in Figure 12) is defined as the ratio of Baseline cases (pure noise) falsely classified as signal detection to the total number of Baseline realizations. The FAP is controlled below the 3σ level for all PTA configurations thanks to our voting system described in subsection IV B.

The detection rate of the common signal is also defined as the number of CURN realizations successfully classified as signal detected divided by the total number of realizations that include the signal. This rate increases rapidly with PTA sensitivity, approaching 100% for the fiducial parameters given in Table I. The detection rate remains higher than 90% for less sensitive PTA configurations, and the minimum number of pulsars needed to have 90% chance of detection while keeping other parameters fixed to their fiducial values is 22 pulsars (left panel of Figure 12). The minimum observation time to pierce the 90% level is 9.4 years (middle panel of Figure 12), while shorter observation time limits the detection chance, and it reaches only 15% for 5 years of observation. Naturally, SGWB with higher characteristic strain amplitude has a higher chance of detection than fainter signals, and the lowest strain amplitude to get 90% detection rate of common signal is 1×10^{-15} (right panel of Figure 12).

Upon confirmation of the detection of a common signal, further classification of the signal spatial correlation pattern is essential. We assert the detection of SGWB within 3σ credibility level only if an HD-pattern is recognized, as described in our strategy illustrated in Figure 11. The blue solid lines depicted in Figure 12 show the detection rate and FAP of SGWB with respect to PTA parameters. Similar to the common signal, the FAP of SGWB is defined as the ratio of non-HD (Monopole, Dipole) or CURN realizations that are misclassified as HD to the total number of non-HD/CURN cases.

The FAP for less sensitive PTA configurations lies higher than 3σ level, as the discrimination between the non-HD and HD cases is diminished due to the significant overlap of their feature vectors distributions, specifically the components of $\mathbf{V}_{\text{non-HD}} : \{s_\omega, \mu_\omega\}$ and $\mathbf{V}_{\text{HD}} : \{\sigma_\omega\}$. By enhancing the sensitivity of PTA, specifically through the addition of more pulsars, extending the observation duration, and/or higher SGWB strain amplitude, the capability of distinguishing signals is restored, resulting in the FAP falling below the 3σ level (right panel of Figure 12). Accordingly, the minimum strain amplitude of SGWB can be detected at 3σ confidence level is $A_{\text{SGWB}} \gtrsim 1.2 \times 10^{-15}$.

Now, we also define the detection rate of SGWB as the ratio of HD realizations successfully identified as HD detections to the total number of HD cases. The HD detection rate reaches high values for a more sensitive PTA configuration, and its value for our fiducial parameters is 91%. The minimum number of pulsars required to achieve 90% level of detection rate (with other parameters fixed to their fiducial values) is 76 pulsars (left panel of Figure 12). Similarly, the minimum observation time to have 90% chance of detection is 14.6 years, and the minimum SGWB strain amplitude is 2.3×10^{-15} (middle and right panels of Figure 12).

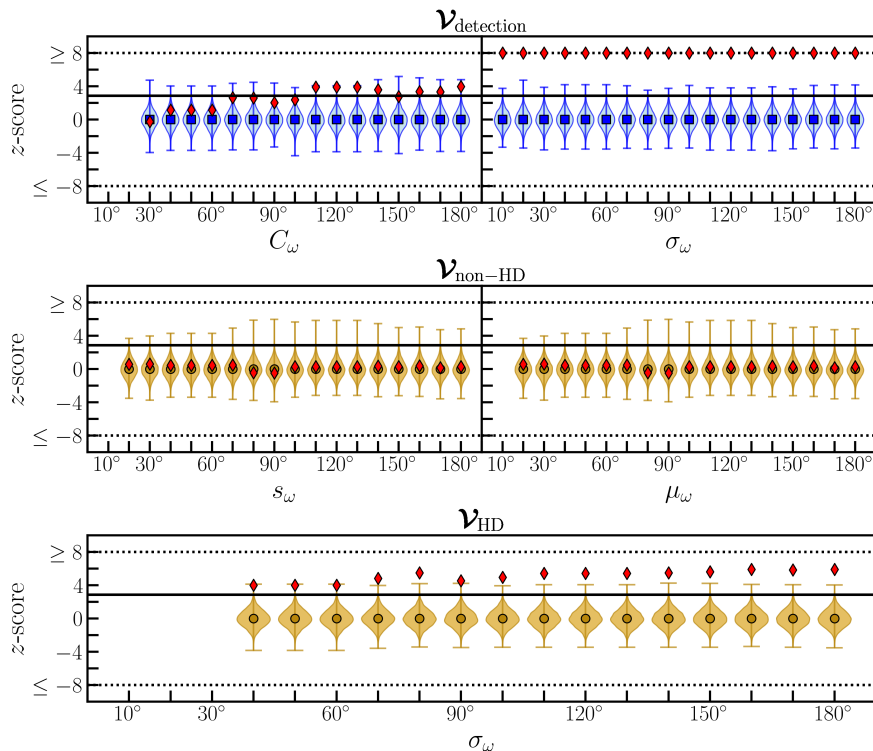


FIG. 13: The merit feature vectors for NG15 dataset (red diamond) compared to the null distributions. Upper panels shows the common signal detection feature vector, $\mathbf{V}_{\text{detection}}$, with Baseline distributions (blue violins). The middle panels correspond to non – HD feature vector, $\mathbf{V}_{\text{non-HD}}$, compared to CURN distributions (golden violins). The merit feature vector of HD detection, \mathbf{V}_{HD} , is shown in the lower panel with CURN distributions overlaid. The z -score triggering thresholds at 2.85σ are demonstrated as black solid lines.

V. QUANTIFYING SGWB INFORMATION CONTENT FROM NG15 DATASET

In the following, we will apply our method on the real PTRs which are publicly available from NANOGrav, the NG15 dataset, which is described in subsection III B and its parameters are summarized in Table I. The PTA constitutes of 68 pulsars observed for 16 years total observation time, indeed not all the pulsars have been observed for the whole time span.

We use the reported noise parameters for individual pulsars extracted by Bayesian noise analysis performed by the NANOGrav team [198]. Relying on these parameters, we simulate 10,000 realizations to compute the Baseline distributions. To construct Baseline + CURN dataset, we perform random phase shuffling on the PTRs resulting in destroying any associated spatial correlation, and finally, by repeating this procedure, we obtain an ensemble of realizations which are necessary for further analysis. Figure 13 shows the implementation of our detection pipeline on the NG15 dataset. The first row depicts the comparison between elements of $\mathbf{V}_{\text{detection}}$ as a function of ζ for Baseline and real data. The NG15 dataset show significantly higher clustering coefficient C_ω than the Baseline distributions for angular separa-

tion thresholds higher than 110° . The standard deviation of edge weights, σ_ω , are clearly higher than the Baseline estimation. the total number of triggered features of $\mathbf{V}_{\text{detection}}$ is 25 out of 34 corresponds to 74% of the features. According to the adopted voting mechanism, we can report a high evidence ($> 3\sigma$) of common signal in the NG15 dataset within our graph-based detection pipeline.

To investigate the nature of the identified common signal, we proceed the evaluation process by computing the elements of the merit feature vector of non – HD patterns, $\mathbf{V}_{\text{non-HD}}$. We compare the $\mathbf{V}_{\text{non-HD}}$ for real data with corresponding Baseline + CURN distributions which is demonstrated in the second row of Figure 13. The z -score for every component of the feature vector related to non – HD patterns is lower than the given threshold, which excludes the Monopole/Dipole spatial pattern hypotheses.

To elucidate the presence of SGWB, we calculate the \mathbf{V}_{HD} for the NG15 dataset. By comparing it with Baseline + CURN, our result is depicted in the last row of Figure 13. The edge weights values of real data demonstrate a higher level of diversity than Baseline + CURN for all angular separation thresholds and 100% of the merit feature vector \mathbf{V}_{HD} are activated. Therefore, we

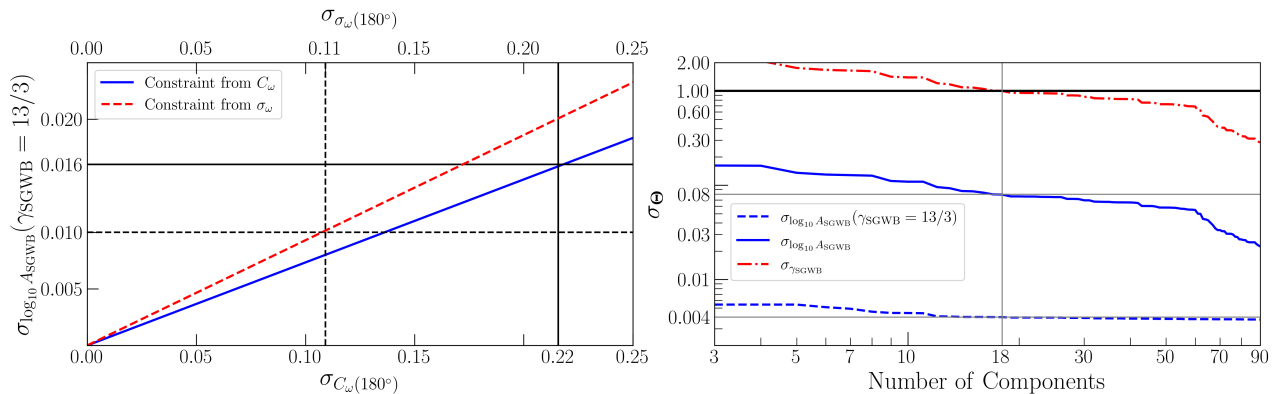


FIG. 14: left panel: The relative statistical error, $\sigma_{\log_{10} A_{\text{SGWB}}}$ for the fiducial value $\Theta_{\text{fiducial}} : \{\log_{10} A_{\text{SGWB}}^{\text{fiducial}} = -14.6, \gamma_{\text{SGWB}}^{\text{fiducial}} = 13/3\}$ as a function of error associated with C_ω (blue solid line) and σ_ω (red dashed line). The vertical solid line corresponds to the 22% relative error of C_ω leading to 1.6% relative error on the $\log_{10} A_{\text{SGWB}}$ at the fiducial point. The vertical dashed line shows the 11% relative error of σ_ω , which is associated with 1% relative error on the $\log_{10} A_{\text{SGWB}}$. The value of relative errors adopted for C_ω and σ_ω in this plot has been computed at fiducial value for 95% credibility level. Here we took $\bar{\zeta} = 180^\circ$. right panel: The blue dashed line and the blue solid line display relative statistical error of $\log_{10} A_{\text{SGWB}}$ for the cases with and without marginalization over the spectral index, respectively. While the red dash-dot line depicts the relative uncertainty of SGWB spectral index marginalized over $\log_{10} A_{\text{SGWB}}$. The solid vertical line corresponds to taking into account the first 18 principal components such that the $\sigma_{\gamma_{\text{SGWB}}} = 100\%$.

obtain significant evidence ($> 3\sigma$) for SGWB detection in NG15 using graph-based summary statistics. We also argue that the graph-based method constitutes a consistent success alongside the Bayesian approach employed by the NANOGrav team. [199].

To extract cosmological information and put pristine constraints on the SGWB model free parameters, $\Theta : \{\log_{10} A_{\text{SGWB}}, \gamma_{\text{SGWB}}\}$, through the graph-based feature vector, \mathcal{G} , and due to its highly non-linear dependency to desired parameters, we need to set up proper emulator for model prediction. Subsequently, we are unable to theoretically mapping the \mathcal{G} to Θ . A feasible way is training a Gaussian process emulator [186] such that a machine learning procedure is adopted to predict distribution of feature vector for arbitrary parameters in training range. Similar method has been utilized in some cosmological inferences through topological data analysis e.g. [200–202]. Another robust approach to cosmological inference is simulation-based inference (SBI). This method is also known as likelihood independent inference. Particularly, for our purpose and by using the kind of our feature vector, the SBI is highly recommended for achieving reliable parameter estimation [124–128, and references therein]. According to either appropriate emulator or SBI, we can use NG15 dataset and by computing the data vector which is \mathcal{G} as new observable quantity to infer parameter estimation and their uncertainties. Alternatively, here we carry out the error propagator framework to clarify the level of uncertainty in measuring $\log_{10} A_{\text{SGWB}}$ and γ_{SGWB} when the graph-based feature vector used as new observable measures. The statistical relative error on de-

sired parameters is given by:

$$\sigma_\Theta^2 = \left(\frac{\partial \ln \mathcal{G}}{\partial \ln \Theta} \right)^{-2} \sigma_\mathcal{G}^2 \quad (25)$$

here σ_Θ and $\sigma_\mathcal{G}$ are relative statistical error of cosmological parameters and error associate with each element of our graph-based data vector, respectively. The relative uncertainty level of $\log_{10} A_{\text{SGWB}}$ with fixed value of γ_{SGWB} at fiducial value propagating from $C_\omega(180^\circ)$ and $\sigma_\omega(180^\circ)$ are shown as the blue solid line and red dashed line in the left panel of Figure 14, respectively. The vertical solid line corresponds to the 22% relative error of C_ω leading to 1.6% relative error on the $\log_{10} A_{\text{SGWB}}$ at the fiducial point. The vertical dashed line shows the 11% relative error of σ_ω , which is associated with 1% relative error on the $\log_{10} A_{\text{SGWB}}$. The value of relative errors adopted for C_ω and σ_ω in this plot has been computed at fiducial value for 95% credibility level.

To get linearly independent components from our feature vector \mathcal{G} , we apply principal component analysis (PCA) [203]. Thus, we consider the principal components extracted by PCA as the feature vector, $\mathcal{A} : \{PC_i\}$, $i = 1, \dots, 90$, instead. Taking into account propagated uncertainties through a new set of data vectors, we compute the relative uncertainty on the $\log_{10} A_{\text{SGWB}}$ given $\gamma_{\text{SGWB}} = 13/3$ as a function of the accumulative number of components in the right panel of Figure 14. The blue dashed line represents the relative statistical error of $\log_{10} A_{\text{SGWB}}$ for $\gamma_{\text{SGWB}} = 13/3$. The blue solid line indicates the $\sigma_{\log_{10} A_{\text{SGWB}}}$ marginalized over γ_{SGWB} . Whereas the red dash-dot line depicts the relative uncertainty of SGWB spectral index marginalized over $\log_{10} A_{\text{SGWB}}$. The solid vertical line corresponds

to taking into account the first 18 principal components where $\sigma_{\gamma_{\text{SGWB}}}$ falls below 100% level. This means that at least 18 of the largest principal components are necessary to constrain the γ_{SGWB} . We also get 8% and 0.4% relative uncertainties of $\log_{10} A_{\text{SGWB}}$ for the cases with and without marginalization over the spectral index, respectively.

Now, relying on the Fisher information matrix, we quantify the capability of graph-based measure and their combination through PCA method on constraining SGWB parameters, Θ . The Fisher information matrix element is given by:

$$F_{\alpha\beta} = \frac{\partial \mathcal{A}^T}{\partial \Theta_\alpha} \mathbf{C}^{-1} \frac{\partial \mathcal{A}}{\partial \Theta_\beta}, \quad (26)$$

where \mathbf{C} is the covariance matrix. To estimate the unbiased covariance matrix, we apply the standard correction on \mathbf{C} as [204]:

$$\mathbf{C}_{\text{unbiased}}^{-1} = \frac{N_{\text{sim}} - N_{\text{tot}} - 2}{N_{\text{sim}} - 1} \mathbf{C}^{-1}, \quad (27)$$

where $N_{\text{sim}} = 10,000$ and N_{tot} is equal to the dimensionality of the feature vector \mathcal{A} . The minimum number of principal components to pierse the 100% relative error threshold on the spectral index is 18 (right panel of Figure 14); we begin our investigation with a data vector with the same dimension. The blue solid lines are devoted to the marginalized likelihood of SGWB parameters when the first 18 principal components are taken into account in Figure 15. If we include all elements of \mathcal{A} for Fisher forecast, the marginalized confidence contours for $\log_{10} A_{\text{SGWB}}$ and γ_{SGWB} become more stringent as indicated by dark red (68%) and light red (95%) contours in Figure 15. For this case, the optimistic uncertainty levels of $\log_{10} A_{\text{SGWB}}$ and γ_{SGWB} reach 2.2% and 28.3%, respectively, at 2σ confidence interval. The posterior of A_{SGWB} for $\gamma_{\text{SGWB}} = 13/3$ is shown via the green dashed line. It is worth noting that an increasing number of components can not change the degeneracy between SGWB strain amplitude and spectral index.

The Fisher forecast through the graph-based summary statistics can provide constraints on SGWB parameters which is in agreement with the Bayesian inference. We advocate that our data-driven approach can be considered as a complementary method for PTA data analysis for both SGWB detection and associated parameters estimation.

VI. SUMMARY AND CONCLUSION

The SGWB that exists in the entire space-time leaves an intrinsic imprint on the PTRs of pulsar timing arrays. This fingerprint is quantified with a distinctive spatial correlation pattern known as Hellings & Downs, and it follows a quasi-quadrupolar behavior with respect to the angular separation between the pulsars. The most sensitive pulsars, MSPs, can achieve high timing precision

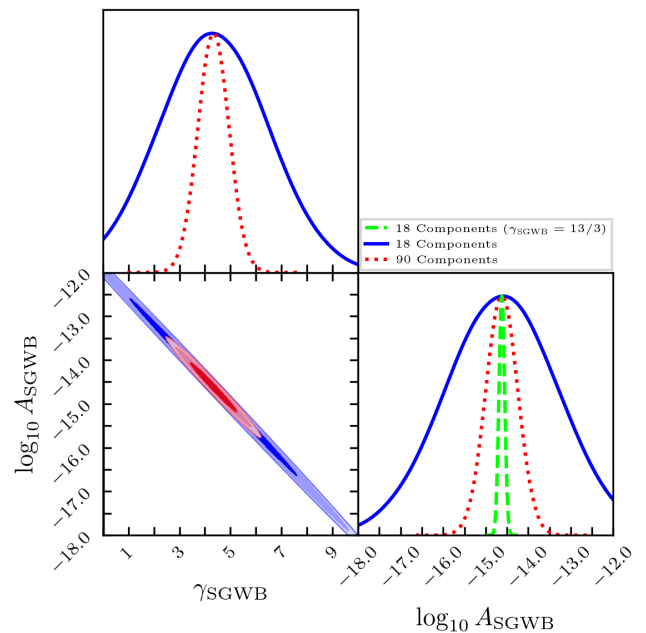


FIG. 15: The constraints on $\log_{10} A_{\text{SGWB}}$ and γ_{SGWB} for 18 principal components (blue contours) and 90 principal components (red contours) in the framework of Fisher forecast. The marginalized posteriors of $\log_{10} A_{\text{SGWB}}$ (lower right panel) and γ_{SGWB} (upper panel) show how adding more features increase the constraining power of graph-based summary statistics. Blue lines represents the posteriors using 18 components and red dotted lines depicts the posteriors using 90 components. The posterior of $\log_{10} A_{\text{SGWB}}$ for $\gamma_{\text{SGWB}} = 13/3$.

capable of detecting the faint signal of SGWB among the noise components sourced by systematic errors and various astrophysical phenomena.

In this work, we developed and tested a novel pipeline for SGWB detection and characterization using graph-based summary statistics derived from PTA data (Figure 1). A goal of this approach is to convert the PTA data into complex networks and extract the structural behavior of the connections by means of graph-based summary statistics to discriminate between various correlation models, specifically monopole, dipole, CURN, and HD spatial correlation patterns.

Our analysis begins with the generation of synthetic PTA data to examine the proposed data-analysis technique on a controlled dataset. The PTRs (Eqs. (1) and (12)) contain white noise sourced by the systematic errors of the telescope, red noise which is caused by the pulsars' phase jitters, and various interstellar medium effects which generate per-pulsar frequency-dependent noise components, and finally the HD correlated SGWB signal. However, other correlation patterns like monopole, caused by the systematic clock errors, and CURN, which introduces an uncorrelated common signal between the pulsars, are injected for comparison

purposes (Figure 4). In addition to mock data, we have used the NANOGrav 15-year dataset (Table I).

To establish the graph-based detection pipeline, we converted the PTA data into graphs by treating the pulsars as the nodes of the graphs and inter-pulsar cross-correlations as the weights of the edges (Figure 5). For each graph (Figures 6 and 8), we computed five graph-based measures that quantify the topological and geometrical properties of the graph, represented as graph-based summary statistics: $\mathcal{G} = \{C_\omega, s_\omega, r_\omega, \mu_\omega, \sigma_\omega\}$.

We employed three statistical metrics to evaluate the discrimination capability of each graph measure, namely *AUC*, Welch's *t*-test *p*-value and Cohen's *d*, over the empirical distributions of graph-based summary statistics (Figure 9) computed from 10,000 realizations of mock data. By adopting the merit feature vectors, our results demonstrated that the average clustering coefficient and the standard deviation of edge weights can significantly distinguish between the Baseline (pure noise) and Baseline + CURN cases as depicted in the upper panel of Figure 10. The average node strengths and the edge weight mean were appropriate indicators for monopole and dipole identification (middle panel of Figure 10). The main and sole indicator of HD was the standard deviation of edge weights (lower panel of Figure 10).

We developed the decision strategy (Figure 11) in such a way that upon observing the imprint of a common signal in the PTRs, we proceed to investigate the nature of the signal. Should the HD correlation pattern be approved after excluding other spatial patterns, we claim a detection of SGWB.

The behavior of the detection rate and false alarm probability (FAP) versus the number of pulsars, observation time span, and the A_{SGWB} (Figure 12) have been investigated. Our results exhibited the lowest detectable value of strain amplitude of SGWB utilizing our graph-based measures is $A_{\text{SGWB}} \gtrsim 1.2 \times 10^{-15}$.

Finally, we evaluated the potential of our graph-based approach for constraining SGWB source parameters by implementing it on real PTA data, the NANOGrav 15-year (NG15) dataset. We found a strong evidence for SGWB within the 3σ credibility level using graph-based summary statistics in the NG15 dataset (Figure 13) which aligns with the finding of [199]. By applying the error propagation method, we computed the statistical relative error of SGWB parameters through the uncertainty propagation of graph-based summary statistics. Assuming the relative uncertainties of 22% and 11% for $C_\omega(180^\circ)$ and $\sigma_\omega(180^\circ)$, the resulting relative errors on $\log_{10} A_{\text{SGWB}}$ are 1.6% and 1.0%, respectively (left panel of Figure 14).

Combining the principal components analysis with the Fisher forecast framework revealed that at least 18 of the largest principal components are necessary to constrain the γ_{SGWB} , which also resulted in the relative error on $\log_{10} A_{\text{SGWB}}$ approaching 8%. Constraining the strain amplitude of SGWB was enhanced by 72 percent when all principal components are taken into account, com-

pared to the case where the largest 18 components are used (Figure 15). The optimistic uncertainty levels of $\log_{10} A_{\text{SGWB}}$ and γ_{SGWB} reached 2.2% and 28.3%, respectively, at 2σ confidence interval.

In summary, our study shows that converting PTA data into a graph enables both detection and characterization of the SGWB through interpretable and computationally efficient summary statistics. While further refinement is needed, especially in the areas of feature selection and parameter estimation, our results motivate continued development of graph-based methods as a complementary tool in the gravitational wave data analysis techniques.

To go further, we suggest to do following tasks as the complementary subjects in the banner of data-driven approaches and SGWB and will be left for the future study: while the correlation graph was a suitable choice to convert the data into a graph, but still the visibility graph method [170], Topological-based data analysis [151–153, 205–208] would be an interesting approach to be examined. Exploring the contribution of different theoretical models in elucidating the SGWB through the Bayesian Model Averaging combined with graph-based analysis is intriguing for signal interpretation [48, 209, 210].

As mentioned in section V, since the highly nonlinear relationship between graph-based summary statistics and SGWB parameters, it is essential to set up a proper emulator for parameter estimation when we are dealing with observed data. The Gaussian Processes Regression (GPR) and other complementary neural density estimators to compute the posterior distribution of the model free parameters should be carried out [124, 125, 126, 127, 128, 200–202, and references therein]. One can enhance the data-driven pipeline by combining it with Machine Learning [211] to get a more sensitive, faster, and robust detection pipeline.

Acknowledgments

The authors are very grateful to M. H. Jalali Kanafi for his extremely useful comments on different parts of this paper. We also thank the NANOGrav team for sharing their data sets and providing extensive instructions on how to utilize the data. The graph-based calculations were performed by using `NetworkX` python package [212]. Also, the Fisher forecast plots are provided by utilizing `Getdist` python package [213]

Appendix A: SGWB Signal Generation via Eigenvalue Decomposition

To simulate timing residuals with specified spatial correlations, we employ eigenvalue decomposition of the tar-

get correlation matrix C :

$$C = Q\Lambda Q^T, \quad (\text{A1})$$

where Q contains eigenvectors and Λ is the diagonal eigenvalue matrix.

We generate N_{PTA} independent Gaussian time series Z with the SGWB power spectrum (Eq. 15). The correlated residuals are constructed as:

$$S_{\text{SGWB}}(t) = Q\Lambda^{1/2}Z. \quad (\text{A2})$$

To ensure positive definiteness, we introduce a small perturbation $\epsilon = |\min\{0, \min(\Lambda)\}|$ and modify the eigenvalues:

$$\tilde{\Lambda} = \Lambda + \text{diag}(\epsilon). \quad (\text{A3})$$

A normalization factor $\rho = \text{diag}(1/(1+\epsilon))$ compensates for the enhanced auto-correlation:

$$S_{\text{SGWB}}(t) = \rho Q\tilde{\Lambda}^{1/2}Z. \quad (\text{A4})$$

-
- [1] A. A. Penzias and R. W. Wilson. A Measurement of Excess Antenna Temperature at 4080 Mc/s. *Astrophysical Journal*, 142:419–421, July 1965.
- [2] Planck Collaboration. Planck 2018 results. I. Overview and the cosmological legacy of Planck. *Astronomy and Astrophysics*, 641:A1, September 2020.
- [3] P.J.E. Peebles. *The Large-Scale Structure of the Universe*. Princeton Series in Physics. Princeton University Press, 2020.
- [4] F. Bernardeau, S. Colombi, E. Gaztañaga, and R. Scoccimarro. Large-scale structure of the universe and cosmological perturbation theory. *Physics Reports*, 367(1):1–248, 2002.
- [5] Ray W. Klebesadel, Ian B. Strong, and Roy A. Olson. Observations of Gamma-Ray Bursts of Cosmic Origin. In E. Fenimore and M. Galassi, editors, *Gamma-Ray Bursts: 30 Years of Discovery*, volume 727 of *American Institute of Physics Conference Series*, pages 3–6. AIP, September 2004.
- [6] Orlando Luongo and Marco Muccino. A Roadmap to Gamma-Ray Bursts: New Developments and Applications to Cosmology. *Galaxies*, 9(4):77, October 2021.
- [7] E. Schreier, R. Levinson, H. Gursky, E. Kellogg, H. Tananbaum, and R. Giacconi. Evidence for the Binary Nature of Centaurus X-3 from UHURU X-Ray Observations. *Astrophysical Journal Letters*, 172:L79, March 1972.
- [8] H. Schatz and K. E. Rehm. X-ray binaries. *Nuclear Physics A*, 777:601–622, October 2006.
- [9] A. Hewish, S. J. Bell, J. D. H. Pilkington, P. F. Scott, and R. A. Collins. Observation of a Rapidly Pulsating Radio Source. *Nature*, 217(5130):709–713, February 1968.
- [10] A. Philippov and M. Kramer. Pulsar Magnetospheres and Their Radiation. *Annual Review of Astron and Astrophys*, 60:495–558, August 2022.
- [11] Maarten Schmidt. Spectrum of a Stellar Object Identified with the Radio Source 3c 286. *Astrophysical Journal*, 136:684, September 1962.
- [12] Albert Einstein. Näherungsweise Integration der Feldgleichungen der Gravitation. *Sitzungsberichte der Königlich Preussischen Akademie der Wissenschaften*, pages 688–696, January 1916.
- [13] Albert Einstein. Über Gravitationswellen. *Sitzungsberichte der Königlich Preussischen Akademie der Wissenschaften*, pages 154–167, January 1918.
- [14] S. W. Hawking, W. Israel, and B. Dolan. Book-Review - Three Hundred Years of Gravitation. *Irish Astronomical Journal*, 21:161, September 1993.
- [15] B. Allen. The Stochastic Gravity-Wave Background: Sources and Detection. In Jean-Alain Marck and Jean-Pierre Lasota, editors, *Relativistic Gravitation and Gravitational Radiation*, pages 373–417, January 1997.
- [16] B. S. Sathyaprakash and Bernard F. Schutz. Physics, Astrophysics and Cosmology with Gravitational Waves. *Living Reviews in Relativity*, 12(1):2, December 2009.
- [17] Chiara Caprini and Daniel G. Figueroa. Cosmological backgrounds of gravitational waves. *Classical and Quantum Gravity*, 35(16):163001, August 2018.
- [18] Nelson Christensen. Stochastic gravitational wave backgrounds. *Reports on Progress in Physics*, 82(1):016903, January 2019.
- [19] B. P. Abbott et al. Observation of Gravitational Waves from a Binary Black Hole Merger. *Physical Review Letters*, 116(6):061102, February 2016.
- [20] V. Mandic, E. Thrane, S. Giampanis, and T. Regimbau. Parameter Estimation in Searches for the Stochastic Gravitational-Wave Background. *Physical Review Letters*, 109(17):171102, October 2012.
- [21] B. P. Abbott et al. An upper limit on the stochastic gravitational-wave background of cosmological origin. *Nature*, 460(7258):990–994, August 2009.
- [22] Nick van Remortel, Kamiel Janssens, and Kevin Turbang. Stochastic gravitational wave background: Methods and implications. *Progress in Particle and Nuclear Physics*, 128:104003, January 2023.
- [23] B. Allen. Stochastic gravity-wave background in inflationary-universe models. *Physical Review D*, 37(8):2078–2085, April 1988.
- [24] M. C. Guzzetti, N. Bartolo, M. Liguori, and S. Matarrese. Gravitational waves from inflation. *Nuovo Cimento Rivista Serie*, 39(9):399–495, August 2016.
- [25] Guillem Domènech. Scalar Induced Gravitational Waves Review. *Universe*, 7(11):398, October 2021.
- [26] Chen Yuan and Qing-Guo Huang. A topic review on probing primordial black hole dark matter with scalar induced gravitational waves. *iScience*, 24(8):102860, August 2021.
- [27] Gianmassimo Tasinato. Stochastic approach to gravitational waves from inflation. *Physical Review D*, 105(2):023521, January 2022.
- [28] Misao Sasaki. Primordial black holes and gravitational waves from inflation. *General Relativity and Gravitation*, 57(5):82, May 2025.
- [29] Tanmay Vachaspati and Alexander Vilenkin. Gravitational radiation from cosmic strings. *Physical Review*

- D*, 31(12):3052–3058, June 1985.
- [30] A. Vilenkin. Cosmic strings and domain walls. *Physics Reports*, 121(5):263–315, January 1985.
- [31] M. B. Hindmarsh and T. W. B. Kibble. Cosmic strings. *Reports on Progress in Physics*, 58(5):477–562, May 1995.
- [32] Thibault Damour and Alexander Vilenkin. Gravitational wave bursts from cusps and kinks on cosmic strings. *Physical Review D*, 64(6):064008, September 2001.
- [33] Jose J. Blanco-Pillado, Ken D. Olum, and Benjamin Shlaer. Large parallel cosmic string simulations: New results on loop production. *Physical Review D*, 83(8):083514, April 2011.
- [34] Christophe Ringeval and Teruaki Suyama. Stochastic gravitational waves from cosmic string loops in scaling. *Journal of Cosmology and Astroparticle Physics*, 2017(12):027, December 2017.
- [35] Jose J. Blanco-Pillado and Ken D. Olum. Stochastic gravitational wave background from smoothed cosmic string loops. *Physical Review D*, 96(10):104046, November 2017.
- [36] Mark Hindmarsh and Jun'ya Kume. Multi-messenger constraints on Abelian-Higgs cosmic string networks. *Journal of Cosmology and Astroparticle Physics*, 2023(4):045, April 2023.
- [37] Andrea Maselli, Stefania Marassi, Valeria Ferrari, Kostas Kokkotas, and Raffaella Schneider. Constraining Modified Theories of Gravity with Gravitational-Wave Stochastic Backgrounds. *Physical Review Letters*, 117(9):091102, August 2016.
- [38] M. Maggiore. Gravitational wave experiments and early universe cosmology. *Physics Reports*, 331(6):283–367, July 2000.
- [39] Pau Amaro-Seoane et al. Laser Interferometer Space Antenna. *arXiv e-prints*, page arXiv:1702.00786, February 2017.
- [40] R. Abbott et al. All-sky search for long-duration gravitational-wave bursts in the third Advanced LIGO and Advanced Virgo run. *Physical Review D*, 104(10):102001, November 2021.
- [41] M. Punturo et al. The Einstein Telescope: a third-generation gravitational wave observatory. *Classical and Quantum Gravity*, 27(19):194002, October 2010.
- [42] Seiji Kawamura et al. Current status of space gravitational wave antenna DECIGO and B-DECIGO. *Progress of Theoretical and Experimental Physics*, 2021(5):05A105, May 2021.
- [43] Sheila Dwyer, Daniel Sigg, Stefan W. Ballmer, Lisa Barsotti, Nergis Mavalvala, and Matthew Evans. Gravitational wave detector with cosmological reach. *Physical Review D*, 91(8):082001, April 2015.
- [44] David Reitze, LIGO Laboratory: California Institute of Technology, LIGO Laboratory: Massachusetts Institute of Technology, LIGO Hanford Observatory, and LIGO Livingston Observatory. The US Program in Ground-Based Gravitational Wave Science: Contribution from the LIGO Laboratory. *Bulletin of the AAS*, 51(3):141, May 2019.
- [45] M. A. McLaughlin. The North American Nanohertz Observatory for Gravitational Waves. *Classical and Quantum Gravity*, 30(22):224008, November 2013.
- [46] P. Demorest et al. The North American Nanohertz Observatory for Gravitational Waves. In *American Astronomical Society Meeting Abstracts*, volume 237 of *American Astronomical Society Meeting Abstracts*, page 101.01, January 2021.
- [47] Timothy Dolch et al. The Student Teams of Astrophysics ResearcherS (STARS) Undergraduate Program in the North American Nanohertz Observatory for Gravitational Waves. In *American Astronomical Society Meeting #240*, volume 240 of *American Astronomical Society Meeting Abstracts*, page 315.01, June 2022.
- [48] Adeela Afzal et al. The NANOGrav 15 yr Data Set: Search for Signals from New Physics. *Astrophysical Journal Letters*, 951(1):L11, July 2023.
- [49] George Hobbs. The Parkes Pulsar Timing Array Project. *Publication of Korean Astronomical Society*, 30(2):577–581, September 2015.
- [50] Matthew Kerr et al. The Parkes Pulsar Timing Array project: second data release. *Publications of the Astron. Soc. of Australia*, 37:e020, June 2020.
- [51] Andrew Zic et al. The Parkes Pulsar Timing Array third data release. *Publications of the Astron. Soc. of Australia*, 40:e049, December 2023.
- [52] R. N. Manchester et al. The Parkes Pulsar Timing Array Project. *Publications of the Astron. Soc. of Australia*, 30:e017, January 2013.
- [53] Michael Kramer and David J. Champion. The European Pulsar Timing Array and the Large European Array for Pulsars. *Classical and Quantum Gravity*, 30(22):224009, November 2013.
- [54] G. Desvignes et al. High-precision timing of 42 millisecond pulsars with the European Pulsar Timing Array. *Monthly Notices of the RAS*, 458(3):3341–3380, May 2016.
- [55] Bhal Chandra Joshi et al. Precision pulsar timing with the ORT and the GMRT and its applications in pulsar astrophysics. *Journal of Astrophysics and Astronomy*, 39(4):51, August 2018.
- [56] G. Hobbs et al. The International Pulsar Timing Array project: using pulsars as a gravitational wave detector. *Classical and Quantum Gravity*, 27(8):084013, April 2010.
- [57] J. P. W. Verbiest et al. The International Pulsar Timing Array: First data release. *Monthly Notices of the RAS*, 458(2):1267–1288, May 2016.
- [58] J. M. Cordes, M. Kramer, T. J. W. Lazio, B. W. Stappers, D. C. Backer, and S. Johnston. Pulsars as tools for fundamental physics & astrophysics. *New Astronomy Review*, 48(11-12):1413–1438, December 2004.
- [59] T. J. W. Lazio. The Square Kilometre Array pulsar timing array. *Classical and Quantum Gravity*, 30(22):224011, November 2013.
- [60] P. E. Dewdney, P. J. Hall, R. T. Schilizzi, and T. J. W. Lazio. The Square Kilometre Array. *IEEE Proceedings*, 97(8):1482–1496, August 2009.
- [61] Rendong Nan and Di Li. The five-hundred-meter aperture spherical radio telescope (FAST) project. In *Materials Science and Engineering Conference Series*, volume 44 of *Materials Science and Engineering Conference Series*, page 012022. IOP, April 2013.
- [62] Arianna I. Renzini, Boris Goncharov, Alexander C. Jenkins, and Patrick M. Meyers. Stochastic Gravitational-Wave Backgrounds: Current Detection Efforts and Future Prospects. *Galaxies*, 10(1):34, February 2022.
- [63] Tania Regimbau, Thomas Dent, Walter Del Pozzo, Ste-

- fanos Giampanis, Tjonnie G. F. Li, Craig Robinson, Chris Van Den Broeck, Duncan Meacher, Carl Rodriguez, B. S. Sathyaprakash, and Katarzyna Wójcik. Mock data challenge for the Einstein Gravitational-Wave Telescope. *Physical Review D*, 86(12):122001, December 2012.
- [64] Tania Regimbau, Duncan Meacher, and Michael Coughlin. Second Einstein Telescope mock science challenge: Detection of the gravitational-wave stochastic background from compact binary coalescences. *Physical Review D*, 89(8):084046, April 2014.
- [65] Karl Wette. SWIGLAL: Python and Octave interfaces to the LALSuite gravitational-wave data analysis libraries. *SoftwareX*, 12:100634, July 2020.
- [66] Gregory Ashton, Moritz Huebner, Paul D. Lasky, Colm Talbot, Kendall Ackley, Sylvia Biscoveanu, Qi Chu, Atul Divarkala, Paul J. Easter, Boris Goncharov, Francisco Hernandez Vivanco, Jan Harms, Marcus E. Lower, Grant D. Meadors, Denyz Melchor, Ethan Payne, Matthew D. Pitkin, Jade Powell, Nikhil Sarin, and Rory J. E. Smith. Bilby: A user-friendly bayesian inference library for gravitational-wave astronomy. *The Astrophysical Journal Supplement Series*, 241(2):27, Apr 2019.
- [67] Antoine Petiteau, Gérard Auger, Hubert Hallowin, Olivier Jeannin, Eric Plagnol, Sophie Pireaux, Tania Regimbau, and Jean-Yves Vinet. LISACode: A scientific simulator of LISA. *Physical Review D*, 77(2):023002, January 2008.
- [68] Justin A. Ellis, Michele Vallisneri, Stephen R. Taylor, and Paul T. Baker. Enterprise: Enhanced numerical toolbox enabling a robust pulsar inference suite, September 2020.
- [69] G. B. Hobbs, R. T. Edwards, and R. N. Manchester. TEMPO2, a new pulsar-timing package - I. An overview. *Monthly Notices of the RAS*, 369(2):655–672, June 2006.
- [70] Jing Luo, Scott Ransom, Paul Demorest, Paul S. Ray, Anne Archibald, Matthew Kerr, Ross J. Jennings, Matteo Bachetti, Rutger van Haasteren, Chloe A. Champagne, Jonathan Colen, Camryn Phillips, Josef Zimmerman, Kevin Stovall, Michael T. Lam, and Fredrick A. Jenet. PINT: A Modern Software Package for Pulsar Timing. *Astrophysical Journal*, 911(1):45, April 2021.
- [71] Androniki Dimitriou, Daniel G. Figueroa, and Bryan Zaldivar. Fast likelihood-free reconstruction of gravitational wave backgrounds. *Journal of Cosmology and Astroparticle Physics*, 2024(9):032, September 2024.
- [72] Nicola Bellomo, Daniele Bertacca, Alexander C. Jenkins, Sabino Matarrese, Alvise Raccanelli, Tania Regimbau, Angelo Ricciardone, and Mairi Sakellariadou. CLASS_GWB: robust modeling of the astrophysical gravitational wave background anisotropies. *Journal of Cosmology and Astroparticle Physics*, 2022(6):030, June 2022.
- [73] Shu-Xu Yi et al. The Gravitational Wave Universe Toolbox. A software package to simulate observations of the gravitational wave universe with different detectors. *Astronomy and Astrophysics*, 663:A155, July 2022.
- [74] Frank Löffler, Joshua Faber, Eloisa Bentivegna, Tanja Bode, Peter Diener, Roland Haas, Ian Hinder, Bruno C. Mundim, Christian D. Ott, Erik Schnetter, Gabrielle Allen, Manuela Campanelli, and Pablo Laguna. The Einstein Toolkit: a community computational infrastructure for relativistic astrophysics. *Classical and Quantum Gravity*, 29(11):115001, June 2012.
- [75] B. F. Schutz. Determining the Hubble constant from gravitational wave observations. *Nature*, 323(6086):310–311, September 1986.
- [76] Daniel E. Holz and Scott A. Hughes. Using Gravitational-Wave Standard Sirens. *Astrophysical Journal*, 629(1):15–22, August 2005.
- [77] B. P. Abbott et al. A gravitational-wave standard siren measurement of the Hubble constant. *Nature*, 551(7678):85–88, November 2017.
- [78] Xin Zhang. Gravitational wave standard sirens and cosmological parameter measurement. *Science China Physics, Mechanics, and Astronomy*, 62(11):110431, November 2019.
- [79] Xuan-Neng Zhang, Ling-Feng Wang, Jing-Fei Zhang, and Xin Zhang. Improving cosmological parameter estimation with the future gravitational-wave standard siren observation from the Einstein Telescope. *Physical Review D*, 99(6):063510, March 2019.
- [80] Rachel Gray, Ignacio Magaña Hernandez, Hong Qi, Ankan Sur, Patrick R. Brady, Hsin-Yu Chen, Will M. Farr, Maya Fishbach, Jonathan R. Gair, Archisman Ghosh, Daniel E. Holz, Simone Mastrogiovanni, Christopher Messenger, Danièle A. Steer, and John Veitch. Cosmological inference using gravitational wave standard sirens: A mock data analysis. *Physical Review D*, 101(12):122001, June 2020.
- [81] Shang-Jie Jin, Ling-Feng Wang, Peng-Ju Wu, Jing-Fei Zhang, and Xin Zhang. How can gravitational-wave standard sirens and 21-cm intensity mapping jointly provide a precise late-universe cosmological probe? *Physical Review D*, 104(10):103507, November 2021.
- [82] Matteo Braglia and Sachiko Kuroyanagi. Probing pre-recombination physics by the cross-correlation of stochastic gravitational waves and CMB anisotropies. *Physical Review D*, 104(12):123547, December 2021.
- [83] Simone Mastrogiovanni, Danny Laghi, Rachel Gray, Giada Caneva Santoro, Archisman Ghosh, Christos Karathanasis, Konstantin Leyde, Danièle A. Steer, Stéphane Perriès, and Grégoire Pierra. Joint population and cosmological properties inference with gravitational waves standard sirens and galaxy surveys. *Physical Review D*, 108(4):042002, August 2023.
- [84] Florian Schulze, Lorenzo Valbusa Dall’Armi, Julien Lesgourgues, Angelo Ricciardone, Nicola Bartolo, Daniele Bertacca, Christian Fidler, and Sabino Matarrese. GW_CLASS: Cosmological Gravitational Wave Background in the cosmic linear anisotropy solving system. *Journal of Cosmology and Astroparticle Physics*, 2023(10):025, October 2023.
- [85] Shang-Jie Jin, Ji-Yu Song, Tian-Yang Sun, Si-Ren Xiao, He Wang, Ling-Feng Wang, Jing-Fei Zhang, and Xin Zhang. Gravitational wave standard sirens: A brief review of cosmological parameter estimation. *arXiv e-prints*, page arXiv:2507.12965, July 2025.
- [86] Donghui Jeong and Fabian Schmidt. Large-scale structure with gravitational waves. I. Galaxy clustering. *Physical Review D*, 86(8):083512, October 2012.
- [87] Fabian Schmidt and Donghui Jeong. Large-scale structure with gravitational waves. II. Shear. *Physical Review D*, 86(8):083513, October 2012.
- [88] Fabian Schmidt, Enrico Pajer, and Matias Zaldarriaga. Large-scale structure and gravitational waves. III. Tidal effects. *Physical Review D*, 89(8):083507, April 2014.

- [89] Fulvio Scaccabarozzi, Jaiyul Yoo, and Sang Gyu Biern. Galaxy two-point correlation function in general relativity. *Journal of Cosmology and Astroparticle Physics*, 2018(10):024, October 2018.
- [90] Pritha Bari, Angelo Ricciardone, Nicola Bartolo, Daniele Bertacca, and Sabino Matarrese. Signatures of Primordial Gravitational Waves on the Large-Scale Structure of the Universe. *Physical Review Letters*, 129(9):091301, August 2022.
- [91] L. Perivolaropoulos and F. Skara. Challenges for Λ CDM: An update. *New Astronomy Review*, 95:101659, December 2022.
- [92] Dominik J. Schwarz, Craig J. Copi, Dragan Huterer, and Glenn D. Starkman. CMB anomalies after Planck. *Classical and Quantum Gravity*, 33(18):184001, September 2016.
- [93] S. Yeung and M. C. Chu. Directional variations of cosmological parameters from the Planck CMB data. *Physical Review D*, 105(8):083508, April 2022.
- [94] Hai-Nan Lin, Jin Li, and Xin Li. Testing the anisotropy of the universe using the simulated gravitational wave events from advanced LIGO and Virgo. *European Physical Journal C*, 78(5):356, May 2018.
- [95] Giacomo Galloni, Nicola Bartolo, Sabino Matarrese, Marina Migliaccio, Angelo Ricciardone, and Nicola Vittorio. Test of the statistical isotropy of the universe using gravitational waves. *Journal of Cosmology and Astroparticle Physics*, 2022(9):046, September 2022.
- [96] N. M. Jiménez Cruz, Ameet Malhotra, Gianmassimo Tasinato, and Ivonne Zavala. Measuring kinematic anisotropies with pulsar timing arrays. *Physical Review D*, 110(6):063526, September 2024.
- [97] Leila L. Graef, Micol Benetti, and Jailson S. Alcaniz. Primordial gravitational waves and the H_0 -tension problem. *Physical Review D*, 99(4):043519, February 2019.
- [98] Meng-Di Cao, Jie Zheng, Jing-Zhao Qi, Xin Zhang, and Zong-Hong Zhu. A New Way to Explore Cosmological Tensions Using Gravitational Waves and Strong Gravitational Lensing. *Astrophysical Journal*, 934(2):108, August 2022.
- [99] Tian-Nuo Li, Shang-Jie Jin, Hai-Li Li, Jing-Fei Zhang, and Xin Zhang. Prospects for Probing the Interaction between Dark Energy and Dark Matter Using Gravitational-wave Dark Sirens with Neutron Star Tidal Deformation. *Astrophysical Journal*, 963(1):52, March 2024.
- [100] Ruth Durrer and Andrii Neronov. Cosmological magnetic fields: their generation, evolution and observation. *Astronomy and Astrophysics Reviews*, 21:62, June 2013.
- [101] Kandaswamy Subramanian. The origin, evolution and signatures of primordial magnetic fields. *Reports on Progress in Physics*, 79(7):076901, July 2016.
- [102] Tanmay Vachaspati. Progress on cosmological magnetic fields. *Reports on Progress in Physics*, 84(7):074901, July 2021.
- [103] Chiara Caprini and Ruth Durrer. Gravitational wave production: A strong constraint on primordial magnetic fields. *Physical Review D*, 65(2):023517, December 2001.
- [104] Andrii Neronov, Alberto Roper Pol, Chiara Caprini, and Dmitri Semikoz. NANOGrav signal from magnetohydrodynamic turbulence at the QCD phase transition in the early Universe. *Physical Review D*, 103(4):L041302, February 2021.
- [105] Alberto Roper Pol, Chiara Caprini, Andrii Neronov, and Dmitri Semikoz. Gravitational wave signal from primordial magnetic fields in the Pulsar Timing Array frequency band. *Physical Review D*, 105(12):123502, June 2022.
- [106] G. Franciolini. Primordial Black Holes: from Theory to Gravitational Wave Observations. *arXiv e-prints*, page arXiv:2110.06815, October 2021.
- [107] Jose J. Blanco-Pillado, Ken D. Olum, and Xavier Siemens. New limits on cosmic strings from gravitational wave observation. *Physics Letters B*, 778:392–396, March 2018.
- [108] Jose J. Blanco-Pillado, Ken D. Olum, and Jeremy M. Wichter. Comparison of cosmic string and superstring models to NANOGrav 12.5-year results. *Physical Review D*, 103(10):103512, May 2021.
- [109] R. Abbott et al. Constraints on Cosmic Strings Using Data from the Third Advanced LIGO–Virgo Observing Run. *Physical Review Letters*, 126(24):241102, June 2021.
- [110] Jun’ya Kume and Mark Hindmarsh. Revised bounds on local cosmic strings from NANOGrav observations. *Journal of Cosmology and Astroparticle Physics*, 2024(12):001, December 2024.
- [111] Kevork Abazajian et al. CMB-S4 Science Case, Reference Design, and Project Plan. *arXiv e-prints*, page arXiv:1907.04473, July 2019.
- [112] Maximilian H. Abitbol et al. CMB-S4 Technology Book, First Edition. *arXiv e-prints*, page arXiv:1706.02464, June 2017.
- [113] George Em Karniadakis, Ioannis G. Kevrekidis, Lu Lu, Paris Perdikaris, Sifan Wang, and Liu Yang. Physics-informed machine learning. *Nature Reviews Physics*, 3(6):422–440, June 2021.
- [114] Zhongkai Hao, Songming Liu, Yichi Zhang, Chengyang Ying, Yao Feng, Hang Su, and Jun Zhu. Physics-Informed Machine Learning: A Survey on Problems, Methods and Applications. *arXiv e-prints*, page arXiv:2211.08064, November 2022.
- [115] Daniel George and E. A. Huerta. Deep Learning for real-time gravitational wave detection and parameter estimation: Results with Advanced LIGO data. *Physics Letters B*, 778:64–70, March 2018.
- [116] Elena Cuoco et al. Enhancing gravitational-wave science with machine learning. *Machine Learning: Science and Technology*, 2(1):011002, January 2021.
- [117] Stefano Schmidt, Matteo Breschi, Rossella Gamba, Giulia Pagano, Piero Rettegno, Gunnar Riemenschneider, Sebastiano Bernuzzi, Alessandro Nagar, and Walter Del Pozzo. Machine learning gravitational waves from binary black hole mergers. *Physical Review D*, 103(4):043020, February 2021.
- [118] Rich Ormiston, Tri Nguyen, Michael Coughlin, Rana X. Adhikari, and Erik Katsavounidis. Noise reduction in gravitational-wave data via deep learning. *Physical Review Research*, 2(3):033066, July 2020.
- [119] G. Vajente, Y. Huang, M. Isi, J. C. Driggers, J. S. Kissel, M. J. Szczepańczyk, and S. Vitale. Machine-learning nonstationary noise out of gravitational-wave detectors. *Physical Review D*, 101(4):042003, February 2020.
- [120] Seiya Sasaoka, Yilun Hou, Kentaro Somiya, and Hirotaka Takahashi. Localization of gravitational waves using machine learning. *Physical Review D*, 105(10):103030, May 2022.
- [121] Alex Kolmus, Grégory Baltus, Justin Janquart, Twan

- van Laarhoven, Sarah Caudill, and Tom Heskes. Fast sky localization of gravitational waves using deep learning seeded importance sampling. *Physical Review D*, 106(2):023032, July 2022.
- [122] Chayan Chatterjee, Linqing Wen, Damon Beveridge, Linqing Wen Team, and Damon Beveridge Team. Real-time localization of gravitational waves from compact binary coalescences using deep learning. In *APS April Meeting Abstracts*, volume 2022 of *APS Meeting Abstracts*, page E17.006, April 2022.
- [123] Elena Cuoco, Marco Cavaglia, Ik Siong Heng, David Keitel, and Christopher Messenger. Applications of machine learning in gravitational-wave research with current interferometric detectors: Applications of machine learning in gravitational-wave... *Living Reviews in Relativity*, 28(1):2, February 2025.
- [124] Alvaro Tejero-Cantero, Jan Boelts, Michael Deistler, Jan-Matthis Lueckmann, Conor Durkan, Pedro Gonçalves, David Greenberg, and Jakob Macke. sbi: A toolkit for simulation-based inference. *The Journal of Open Source Software*, 5(52):2505, August 2020.
- [125] George Papamakarios and Iain Murray. Fast ϵ -free Inference of Simulation Models with Bayesian Conditional Density Estimation. *arXiv e-prints*, page arXiv:1605.06376, May 2016.
- [126] Justin Alsing, Tom Charnock, Stephen Feeney, and Benjamin Wandelt. Fast likelihood-free cosmology with neural density estimators and active learning. *Monthly Notices of the RAS*, 488(3):4440–4458, September 2019.
- [127] Kyle Cranmer, Johann Brehmer, and Gilles Louppe. The frontier of simulation-based inference. *Proceedings of the National Academy of Science*, 117(48):30055–30062, December 2020.
- [128] ChangHoon Hahn, Muntazir Abidi, Michael Eickenberg, Shirley Ho, Pablo Lemos, Elena Massara, Azadeh Moradinezhad Dizgah, and Bruno Régalo-Saint Blancard. SIMBIG: Likelihood-Free Inference of Galaxy Clustering. In *Machine Learning for Astrophysics*, page 24, July 2022.
- [129] James Alvey, Uddipta Bhardwaj, Valerie Domcke, Mauro Pieroni, and Christoph Weniger. Simulation-based inference for stochastic gravitational wave background data analysis. *Physical Review D*, 109(8):083008, April 2024.
- [130] J. R. Bond and G. Efstathiou. The statistics of cosmic background radiation fluctuations. *Monthly Notices of the RAS*, 226:655–687, June 1987.
- [131] Wayne Hu and Scott Dodelson. Cosmic Microwave Background Anisotropies. *Annual Review of Astron and Astrophys*, 40:171–216, January 2002.
- [132] S. Dodelson and F. Schmidt. *Modern Cosmology*. Elsevier Science, 2020.
- [133] Ruth Durrer. *The Cosmic Microwave Background*. Cambridge University Press, 2020.
- [134] J. Lesgourges. Cosmological Perturbations. In Konstantin Matchev and et al., editors, *Searching for New Physics at Small and Large Scales (TASI 2012) - Proceedings of the 2012 Theoretical Advanced Study Institute in Elementary Particle Physics. Edited by Schmaltz Martin & Pierpaoli Elena. Published by World Scientific Publishing Co. Pte. Ltd*, pages 29–97, August 2013.
- [135] Planck Collaboration. Planck 2018 results. VII. Isotropy and statistics of the CMB. *Astronomy and Astrophysics*, 641:A7, September 2020.
- [136] Asantha Cooray and Ravi Sheth. Halo models of large scale structure. *Physics Reports*, 372(1):1–129, December 2002.
- [137] Takahiko Matsubara. Statistics of Smoothed Cosmic Fields in Perturbation Theory. I. Formulation and Useful Formulae in Second-Order Perturbation Theory. *Astrophysical Journal*, 584(1):1–33, February 2003.
- [138] Takahiko Matsubara and Satoshi Kuriki. Weakly non-Gaussian formula for the Minkowski functionals in general dimensions. *Physical Review D*, 104(10):103522, November 2021.
- [139] Robert J Adler. *The Geometry of Random Fields*. Society for Industrial and Applied Mathematics, 2010.
- [140] K. R. Mecke, T. Buchert, and H. Wagner. Robust morphological measures for large-scale structure in the Universe. *Astronomy and Astrophysics*, 288:697–704, August 1994.
- [141] Jens Schmalzing and Thomas Buchert. Beyond Genus Statistics: A Unifying Approach to the Morphology of Cosmic Structure. *Astrophysical Journal Letters*, 482(1):L1–L4, June 1997.
- [142] C. Beisbart, T. Buchert, and H. Wagner. Morphometry of spatial patterns. *Physica A Statistical Mechanics and its Applications*, 293:592–604, April 2001.
- [143] Claus Beisbart, Robert Dahlke, Klaus Mecke, and Herbert Wagner. Vector- and Tensor-Valued Descriptors for Spatial Patterns. In K. Mecke and D. Stoyan, editors, *Morphology of Condensed Matter*, volume 600, pages 238–260. 2002.
- [144] Takahiko Matsubara and Jun'ichi Yokoyama. Genus Statistics of the Large-Scale Structure with Non-Gaussian Density Fields. *Astrophysical Journal*, 463:409, June 1996.
- [145] S. Codis, C. Pichon, D. Pogosyan, F. Bernardeau, and T. Matsubara. Non-Gaussian Minkowski functionals and extrema counts in redshift space. *Monthly Notices of the RAS*, 435(1):531–564, October 2013.
- [146] Stephen Appleby, Pravabati Chingangbam, Changbom Park, Sungwook E. Hong, Juhan Kim, and Vidhya Ganesan. Minkowski Tensors in Two Dimensions: Probing the Morphology and Isotropy of the Matter and Galaxy Density Fields. *Astrophysical Journal*, 858(2):87, May 2018.
- [147] Stephen Appleby, Joby P. Kochappan, Pravabati Chingangbam, and Changbom Park. Ensemble Average of Three-dimensional Minkowski Tensors of a Gaussian Random Field in Redshift Space. *Astrophysical Journal*, 887(2):128, December 2019.
- [148] Stephen Appleby, Joby P. Kochappan, Pravabati Chingangbam, and Changbom Park. Minkowski Tensors in Redshift Space-Beyond the Plane-parallel Approximation. *Astrophysical Journal*, 942(2):110, January 2023.
- [149] M. H. Jalali Kanafi and S. M. S. Movahed. Probing the Anisotropy and Non-Gaussianity in the Redshift Space through the Conditional Moments of the First Derivative. *The Astrophysical Journal*, 963(1):31, March 2024.
- [150] Adeela Afzal, M. Alakhras, M. H. Jalali Kanafi, and S. M. S. Movahed. Cosmic Strings-induced CMB anisotropies in light of Weighted Morphology. *Monthly Notices of the RAS*, July 2025.
- [151] Jacky H. T. Yip, Matteo Biagetti, Alex Cole, Karthik Viswanathan, and Gary Shiu. Cosmology with persistent homology: a Fisher forecast. *Journal of Cosmology and Astroparticle Physics*, 2024(9):034, September

- 2024.
- [152] M. H. Jalali Kanafi, S. Ansarifard, and S. M. S. Movahed. Imprint of massive neutrinos on Persistent Homology of large-scale structure. *Monthly Notices of the RAS*, 535(1):657–674, November 2024.
- [153] Fatemeh Abedi, Mohammad Hossein Jalali Kanafi, and Seyed Mohammad Sadegh Movahed. Impact of redshift space distortions on persistent homology of cosmic matter density field. *International Journal of Geometric Methods in Modern Physics*, 22(10):2540006–143, September 2025.
- [154] D. R. Lorimer and M. Kramer. *Handbook of Pulsar Astronomy*. 2012.
- [155] I. Eghdami, H. Panahi, and S. M. S. Movahed. Multifractal Analysis of Pulsar Timing Residuals: Assessment of Gravitational Wave Detection. *Astrophysical Journal*, 864(2):162, September 2018.
- [156] Scott Ransom, A. Brazier, S. Chatterjee, T. Cohen, J. M. Cordes, M. E. DeCesar, P. B. Demorest, J. S. Hazboun, M. T. Lam, R. S. Lynch, M. A. McLaughlin, S. M. Ransom, X. Siemens, S. R. Taylor, and S. J. Vigeland. The NANOGrav Program for Gravitational Waves and Fundamental Physics. In *Bulletin of the American Astronomical Society*, volume 51, page 195, September 2019.
- [157] R. W. Hellings and G. S. Downs. Upper limits on the isotropic gravitational radiation background from pulsar timing analysis. *Astrophysical Journal Letters*, 265:L39–L42, February 1983.
- [158] Fredrick A. Jenet, George B. Hobbs, K. J. Lee, and Richard N. Manchester. Detecting the Stochastic Gravitational Wave Background Using Pulsar Timing. *Astrophysical Journal Letters*, 625(2):L123–L126, June 2005.
- [159] Kazuya Furusawa, Sachiko Kuroyanagi, and Kiyotomo Ichiki. Resolving Individual Signal in the Presence of Stochastic Background in Future Pulsar Timing Arrays. *arXiv e-prints*, page arXiv:2505.10284, May 2025.
- [160] Reginald Christian Bernardo and Kin-Wang Ng. Stochastic gravitational wave background phenomenology in a pulsar timing array. *Physical Review D*, 107(4):044007, February 2023.
- [161] J. P. Eckmann, S. Oliffson Kamphorst, and D. Ruelle. Recurrence plots of dynamical systems. *EPL (Europhysics Letters)*, 4:973, November 1987.
- [162] Norbert Marwan, M. Carmen Romano, Marco Thiel, and Jürgen Kurths. Recurrence plots for the analysis of complex systems. *Physics Reports*, 438(5-6):237–329, January 2007.
- [163] Hu Zhan. Consideration for a large-scale multi-color imaging and slitless spectroscopy survey on the Chinese space station and its application in dark energy research. *Scientia Sinica Physica, Mechanica & Astronomica*, 41(12):1441, January 2011.
- [164] Cheng-Bang Chen, Hui Yang, and Soundar Kumara. Recurrence network modeling and analysis of spatial data. *Chaos: An Interdisciplinary Journal of Nonlinear Science*, 28(8), 2018.
- [165] Floris Takens. Detecting strange attractors in turbulence. In *Dynamical systems and turbulence, Warwick 1980*, pages 366–381. Springer, 1981.
- [166] Norman H Packard, James P Crutchfield, J Doyne Farmer, and Robert S Shaw. Geometry from a time series. *Physical review letters*, 45(9):712, 1980.
- [167] Audun Myers, Elizabeth Munch, and Firas A. Khasawneh. Persistent homology of complex networks for dynamic state detection. *Physical Review E*, 100(2):022314, August 2019.
- [168] Melih C Yesilli, Firas A Khasawneh, and Andreas Otto. Topological feature vectors for chatter detection in turning processes. *The International Journal of Advanced Manufacturing Technology*, 119(9):5687–5713, 2022.
- [169] Audun D. Myers, Max M. Chumley, Firas A. Khasawneh, and Elizabeth Munch. Persistent homology of coarse-grained state-space networks. *Physical Review E*, 107(3):034303, March 2023.
- [170] Lucas Lacasa, Angel Nunez, Édgar Roldán, Juan MR Parrondo, and Bartolo Luque. Time series irreversibility: a visibility graph approach. *The European Physical Journal B*, 85(6):217, 2012.
- [171] Yue Yang, Jianbo Wang, Huijie Yang, and Jingshi Mang. Visibility graph approach to exchange rate series. *Physica A Statistical Mechanics and its Applications*, 388(20):4431–4437, October 2009.
- [172] Michael Small. Complex networks from time series: Capturing dynamics. In *2013 IEEE International Symposium on Circuits and Systems (ISCAS)*, pages 2509–2512. IEEE, 2013.
- [173] Michael McCullough, Michael Small, Thomas Stemler, and Herbert Ho-Ching Iu. Time lagged ordinal partition networks for capturing dynamics of continuous dynamical systems. *Chaos*, 25(5):053101, May 2015.
- [174] Andriana S. L. O. Campanharo, M. Irmak Sirer, R. Dean Malmgren, Fernando M. Ramos, and Luís A. Nunes. Amaral. Duality between time series and networks. *PLOS ONE*, 6(8):1–13, 08 2011.
- [175] Vanessa Freitas Silva, Maria Eduarda Silva, Pedro Ribeiro, and Fernando Silva. Time series analysis via network science: Concepts and algorithms. *Wiley Interdisciplinary Reviews: Data Mining and Knowledge Discovery*, 11(3):e1404, 2021.
- [176] Yong Zou, Reik V. Donner, Norbert Marwan, Jonathan F. Donges, and Jürgen Kurths. Complex network approaches to nonlinear time series analysis. *Physics Reports*, 787:1–97, January 2019.
- [177] Holger Kantz and Thomas Schreiber. *Nonlinear time series analysis*. Cambridge university press, 2003.
- [178] Dmitri Krioukov, Maksim Kitsak, Robert S. Sinkovits, David Rideout, David Meyer, and Marián Boguñá. Network Cosmology. *Scientific Reports*, 2:793, November 2012.
- [179] Sungryong Hong, Bruno C. Coutinho, Arjun Dey, Albert-L. Barabási, Mark Vogelsberger, Lars Hernquist, and Karl Gebhardt. Discriminating topology in galaxy distributions using network analysis. *Monthly Notices of the RAS*, 459(3):2690–2700, July 2016.
- [180] C. R. García, G. Illiano, D. F. Torres, A. Papitto, F. Coti Zelati, D. de Martino, and A. Patruno. Millisecond pulsars phenomenology under the light of graph theory. *Astronomy and Astrophysics*, 692:A187, December 2024.
- [181] C. R. García, Diego F. Torres, and Alessandro Patruno. Visualizing the pulsar population using graph theory. *Monthly Notices of the RAS*, 515(3):3883–3897, September 2022.
- [182] D. Vohl, J. van Leeuwen, and Y. Maan. Topology of Pulsar Profiles (ToPP). I. Graph theory method and classification of the EPN. *Astronomy and Astrophysics*,

- 687:A113, July 2024.
- [183] Jens Jasche and Benjamin D. Wandelt. Bayesian physical reconstruction of initial conditions from large-scale structure surveys. *Monthly Notices of the RAS*, 432(2):894–913, June 2013.
- [184] Drew Jamieson, Yin Li, Renan Alves de Oliveira, Francisco Villaescusa-Navarro, Shirley Ho, and David N. Spergel. Field-level Neural Network Emulator for Cosmological N-body Simulations. *Astrophysical Journal*, 952(2):145, August 2023.
- [185] Nhat-Minh Nguyen, Fabian Schmidt, Beatriz Tucci, Martin Reinecke, and Andrija Kostić. How Much Information Can Be Extracted from Galaxy Clustering at the Field Level? *Physical Review Letters*, 133(22):221006, November 2024.
- [186] Andrew Gelman, John B. Carlin, Hal S. Stern, David B. Dunson, Aki Vehtari, and Donald B. Rubin. *Bayesian Data Analysis*. 2014.
- [187] Bruce Allen and Adrian C. Ottewill. Detection of anisotropies in the gravitational-wave stochastic background. *Physical Review D*, 56(2):545–563, July 1997.
- [188] Gabriella Agazie et al. The NANOGrav 15 yr Data Set: Observations and Timing of 68 Millisecond Pulsars. *Astrophysical Journal Letters*, 951(1):L9, July 2023.
- [189] Duncan J. Watts and Steven H. Strogatz. Collective dynamics of ‘small-world’ networks. *Nature*, 393(6684):440–442, June 1998.
- [190] Réka Albert and Albert-László Barabási. Statistical mechanics of complex networks. *Rev. Mod. Phys.*, 74:47–97, Jan 2002.
- [191] Jukka-Pekka Onnela, Jari Saramäki, János Kertész, and Kimmo Kaski. Intensity and coherence of motifs in weighted complex networks. *Physical Review E*, 71(6):065103, June 2005.
- [192] Mark Newman. *Networks: An Introduction*. Oxford University Press, 03 2010.
- [193] Lee M. Gunderson and Gecia Bravo-Hermsdorff. Introducing Graph Cumulants: What is the Variance of Your Social Network? *arXiv e-prints*, page arXiv:2002.03959, February 2020.
- [194] U. Pigorsch and M. Sabek. Assortative mixing in weighted directed networks. *Physica A Statistical Mechanics and its Applications*, 604:127850, October 2022.
- [195] J.A. Hanley. The meaning and use of the area under a receiver operating characteristic (roc) curve. *Radiology*, 143:29–36, 05 1982.
- [196] B. L. Welch. The generalization of ‘student’s’ problem when several different population variances are involved. *Biometrika*, 34(1/2):28–35, 1947.
- [197] J. Cohen. *Statistical Power Analysis for the Behavioral Sciences*. Lawrence Erlbaum Associates, 2nd edition, 1988.
- [198] Gabriella Agazie et al. The NANOGrav 15 yr Data Set: Detector Characterization and Noise Budget. *Astrophysical Journal Letters*, 951(1):L10, July 2023.
- [199] Gabriella and Agazie et al. The NANOGrav 15 yr Data Set: Evidence for a Gravitational-wave Background. *Astrophysical Journal Letters*, 951(1):L8, July 2023.
- [200] Sven Heydenreich, Benjamin Brück, and Joachim Harnois-Déraps. Persistent homology in cosmic shear: Constraining parameters with topological data analysis. *Astronomy and Astrophysics*, 648:A74, April 2021.
- [201] Daniela Grandón. *Bayesian Inference for Precision Cosmology: a Machine Learning Approach*. PhD thesis, University of Chile, July 2023.
- [202] José de Jesús Velázquez, Luis A. Escamilla, Purba Mukherjee, and J. Alberto Vázquez. Non-Parametric Reconstruction of Cosmological Observables Using Gaussian Processes Regression. *Universe*, 10(12):464, December 2024.
- [203] Hervé Abdi and Lynne J. Williams. Principal component analysis. *WIREs Computational Statistics*, 2(4):433–459, 2010.
- [204] J. Hartlap, P. Simon, and P. Schneider. Why your model parameter confidences might be too optimistic. Unbiased estimation of the inverse covariance matrix. *Astronomy and Astrophysics*, 464(1):399–404, March 2007.
- [205] Afra J Zomorodian. *Topology for computing*. Cambridge university press, 2005.
- [206] Larry Wasserman. Topological data analysis. *Annual Review of Statistics and Its Application*, 5(Volume 5, 2018):501–532, 2018.
- [207] Tamal Krishna Dey and Yusu Wang. *Computational Topology for Data Analysis*. Cambridge University Press, 2022.
- [208] Herbert Edelsbrunner and J Harer. *Computational Topology: an Introduction*. American Mathematical Society, Providence, R.I., 2010.
- [209] Charlie Hoy. Accelerating multimodel Bayesian inference, model selection, and systematic studies for gravitational wave astronomy. *Physical Review D*, 106(8):083003, October 2022.
- [210] S. Paradiso, M. DiMarco, M. Chen, G. McGee, and W. J. Percival. A convenient approach to characterizing model uncertainty with application to early dark energy solutions of the Hubble tension. *Monthly Notices of the RAS*, 528(2):1531–1540, February 2024.
- [211] S. Adityan and A. Stanley Raj. Tracing gravitational waves by integrating wavelet, PCA and clustering analysis using pulsar timing array data. *Astrophysics and Space Science*, 370(4):35, April 2025.
- [212] Aric A. Hagberg, Daniel A. Schult, and Pieter J. Swart. Exploring network structure, dynamics, and function using networkx. In Gaël Varoquaux, Travis Vaught, and Jarrod Millman, editors, *Proceedings of the 7th Python in Science Conference*, pages 11 – 15, 2008.
- [213] Antony Lewis. GetDist: a Python package for analysing Monte Carlo samples. *JCAP*, 08:025, 2025.